Icarus 202 (2009) 260–279

Contents lists available at ScienceDirect

Icarus

www.elsevier.com/locate/icarus

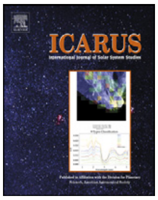

Organizing some very tenuous things: Resonant structures in Saturn's faint rings

M.M. Hedman[a,*], J.A. Burns[a,b], M.S. Tiscareno[a], C.C. Porco[c]

[a] *Department of Astronomy, Cornell University, Ithaca, NY 14853, United States*
[b] *Department of Theoretical and Applied Mechanics, Cornell University, Ithaca, NY 14853, United States*
[c] *CICLOPS-SSI, 4750 Walnut Street, Boulder, CO 80301, United States*

ARTICLE INFO

Article history:
Received 25 November 2008
Revised 19 February 2009
Accepted 24 February 2009
Available online 28 February 2009

Keywords:
Saturn
Planetary rings
Saturn, rings
Resonances, rings

ABSTRACT

Images of the dusty rings obtained by the Cassini spacecraft in late 2006 and early 2007 reveal unusual structures composed of alternating canted bright and dark streaks in the outer G ring (∼170,000 km from Saturn center), the inner Roche Division (∼138,000 km) and the middle D ring (70,000–73,000 km). The morphology, locations and pattern speeds of these features indicate that they are generated by Lindblad resonances. The structure in the G ring appears to be generated by the 8:7 Inner Lindblad Resonance with Mimas. Based in part on the morphology of the G ring structure, we develop a phenomenological model of Lindblad-resonance-induced structures in faint rings, where the observed variations in the rings' optical depth and brightness are due to alignments and trends in the particles' orbital parameters with semi-major axis. To reproduce the canted character of these structures, this model requires a term in the equations of motion that damps eccentricities. Using this model to interpret the structures in the D ring and Roche Division, we find that the D-ring patterns mimic those predicted at 2:1 Inner Lindblad Resonances and the Roche Division patterns look like those expected at 3:4 Outer Lindblad Resonances. As in the G ring, the effective eccentricity-damping timescale is of order 10–100 days, suggesting that free eccentricities are strongly damped by some mechanism that operates throughout all these regions. However, unlike in the G ring, perturbation forces with multiple periods are required to explain the observed patterns in the D ring and Roche Division. The strongest perturbation periods occur at 10.53, 10.56 and 10.74 hours (only detectable in the D ring) and 10.82 hours (detectable in both the D ring and Roche division). These periods are comparable to the rotation periods of Saturn's atmosphere and magnetosphere. The inferred strength of the perturbation forces required to produce these patterns (and the absence of evidence for other resonances driven by these periods in the main rings) suggests that non-gravitational forces are responsible for generating these features in the D ring and Roche Division. If this interpretation is correct, then some of these structures may have some connection with periodic signals observed in Saturn's magnetic field and radio-wave emissions, and accordingly could help clarify the nature and origin(s) of these magnetospheric asymmetries.

0. Introduction

From late 2006 through early 2007, the Cassini spacecraft's tour through the Saturn system carried it into a series of inclined orbits (or "Revs") with apoapses on the opposite side of the planet from the Sun, allowing the rings to be viewed for extended periods of time at very high (∼160°) phase angles. The cameras onboard Cassini were therefore able to obtain multiple sequences of several low-optical-depth rings, including the G ring, the D ring and the Roche Division between the A and F rings. Since these rings are all composed primarily of small (<100 μm), strongly forward-scattering particles, these images had very good signal-to-noise and clearly revealed unusual brightness patterns in all three of these regions. While the morphology of these structures varies somewhat among the different rings, all appear to be composed of alternating bright and dark streaks that are canted relative to the local radial direction. Our investigations of these structures have led us to conclude that all these structures represent the response of dusty rings to Lindblad resonances, and therefore represent a new class of resonant-induced patterns in the rings. Furthermore, while the features in the G ring appear to be generated by a classical Lindblad resonance with a satellite (Mimas), the structures in the D ring and Roche Division instead seem to be due to perturbations tied to the rotation of Saturn's atmosphere and/or magnetic field. The latter therefore may provide important insights into the planet's magnetosphere and interior.

This paper begins by summarizing the imaging sequences used in this analysis (Section 1). Section 2 considers the structure observed in the G ring, presents evidence that it is associated with

---

* Corresponding author.
E-mail address: mmhedman@astro.cornell.edu (M.M. Hedman).

0019-1035/$ – see front matter © 2009 Elsevier Inc. All rights reserved.
doi:10.1016/j.icarus.2009.02.016

Table 1
Imaging sequences used in this analysis.

Ring	Rev/orbit	Images	Image midtimes	Phase angles	Emission angles	Aimpoint longitudes	Note
G ring	029	N1537362584–N1537431998	2006-262T12:37:46–263T07:54:43	162.6°–159.4°	79.9°–81.1°	297.1°–300.0°	
Roche D.	029a	N1538169174–N1538217594	2006-271T20:41:03–272T10:08:03	158.4°–161.7°	57.5°–59.1°	265.9°–269.8°	A
Roche D.	029b	N1538270015–N1538300071	2006-273T00:41:43–273T09:02:39	158.9°–161.0°	60.6°–61.5°	83.3°–85.5°	A
Roche D.	030	N1539655570–N1539683497	2006-289T01:34:10–289T09:19:36	150.6°–152.4°	48.7°–49.7°	265.3°–267.8°	
Roche D.	031	N1541012989–N1541062380	2006-304T18:37:40–305T08:20:51	156.3°–160.3°	51.9°–55.2°	94.7°–99.3°	
Roche D.	032	N1542047155–N1542096546	2006-316T17:53:40–317T07:36:50	155.9°–160.0°	51.8°–55.1°	94.3°–99.1°	
Roche D.	033	N1543166702–N1543217398	2006-329T16:52:39–330T06:57:35	159.8°–160.7°	57.6°–60.7°	294.0°–297.0°	
Roche D.	036	N1545557060–N1545613256	2006-357T08:51:42–358T00:28:18	158.6°–160.8°	54.2°–57.2°	286.3°–290.0°	
D ring	037	N1547138243–N1547168273	2007-010T16:04:35–011T00:25:05	162.2°–162.7°	61.4°–64.1°	295.2°–297.9°	
D ring	039	N1550157993–N1550176627	2007-045T14:53:17–045T20:03:51	161.7°–162.0°	62.7°–65.5°	297.5°–299.4°	B
D ring	043	N1556037232–N1556050246	2007-113T15:59:18–113T12:36:12	140.6°–148.9°	45.5°–51.3°	297.6°–246.0°	

Note: aimpoint longitudes are measured in an inertial longitude system relative to J2000 coordinates. A = only images with longer exposures used. B = only images targeted at the outer D ring (and containing the inner C ring for navigation) used.

the 8:7 ILR with Mimas, and develops a phenomenological model to describe the patterns imposed on a low-optical-depth, dusty ring by a Lindblad resonance. We then turn our attention to the more complex features in the D ring and Roche Division. Section 3 demonstrates that the symmetry properties and pattern speeds of these structures indicate that they are generated by *multiple* resonance-induced patterns and that the perturbation periods are between 10.5 and 10.9 hours. In Section 4 we investigate the dominant periods operating in these regions and in Section 5 we relate these periods to those that have been observed in Saturn's atmosphere and radio emissions.

1. Imaging data

The images discussed here were obtained by the Narrow Angle Camera (NAC) of the Imaging Science Subsystem (ISS) onboard the Cassini spacecraft (Porco et al., 2004). Table 1 lists the imaging sequences discussed in this paper. For all but one of these sequences, the camera pointed at roughly the same radius and inertial longitude in the rings for a significant fraction of the rings' orbital period and took a series of pictures as material rotated through the field of view. The Rev 43 D-ring observation is different from the others in that the camera slewed through ~50° in inertial longitude over the course of the sequence, enabling more material to be seen in a shorter period of time.

All images were initially processed using the CISSCAL calibration routines (Porco et al., 2004) that remove backgrounds, flatfield the images, and convert the raw data numbers into I/F, a standardized measure of reflectance. I is the intensity of the scattered radiation while πF is the solar flux at Saturn, so I/F is a unitless quantity that equals unity for a perfect Lambert surface viewed at normal incidence. In order to facilitate comparisons between observations taken from different elevation angles, we convert the observed I/F values to "normal I/F" $= \mu I/F$, where μ is the cosine of the emission angle. The normal I/F should be independent of emission angle so long as $\tau/\mu \ll 1$ (where τ is the ring's normal optical depth). This condition holds for all the ring features discussed here.

All the images are geometrically navigated using either stars in the field of view (for the G ring sequence) or fiducial features assumed to be circular in the main rings (the inner edge of the C ring for the D ring images and the outer edge of the Keeler gap for the Roche Division data). The imaging data are then reduced into two-dimensional arrays or "maps" of the ring brightness as a function of radius and either longitude in some specified rotating coordinate system or time (assuming the camera stares at a fixed inertial longitude).

For the Roche Division and D ring observations, each image covers a narrow range of longitude compared to the scale of the azimuthal brightness variations. We consequently average the brightness measurements at each radius over longitude to derive a single radial profile from each image. This not only makes the data easier to manipulate but also improves the signal-to-noise of the subtle brightness variations that are under investigation here.

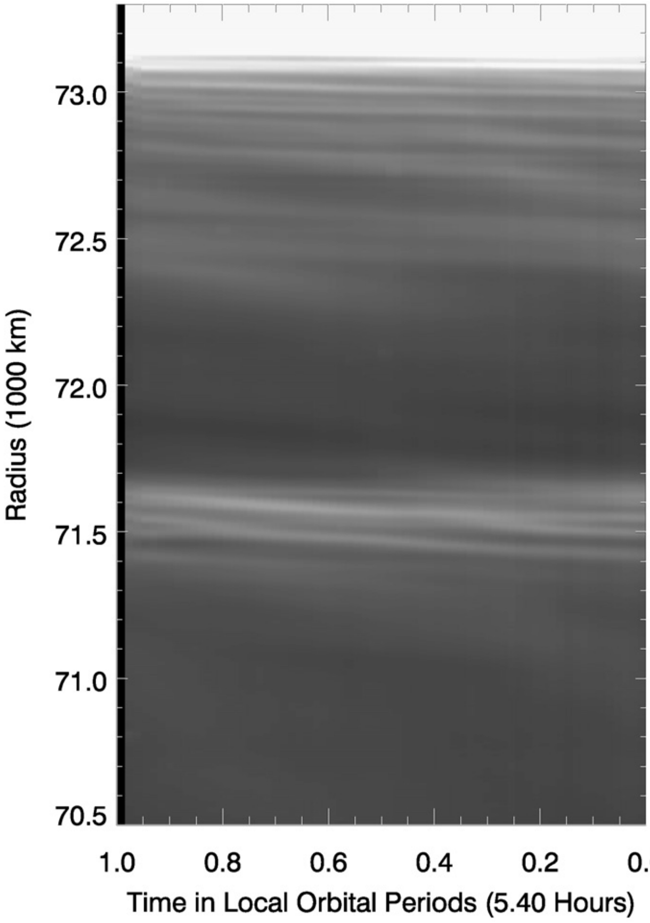

Fig. 1. Map of the middle D ring derived from the Rev 39 sequence, showing the brightness of the ring at an inertial longitude of ~298° versus radius and time. Longitudinal brightness variations can be clearly seen around 71,500 km (i.e., the D72 ringlet) and between 72,500 and 73,000 km (just interior to D73). Note a background that varies linearly with radius has been subtracted from each radial scan used to form this image. Similar maps of this region derived from the other data sets are given in Appendix A (Figs. 19 and 20).

Figs. 1 and 2 show maps of the D ring and Roche Division, each derived from one of the above sets of radial scans (maps derived from the other data sets are given in Appendix A). These

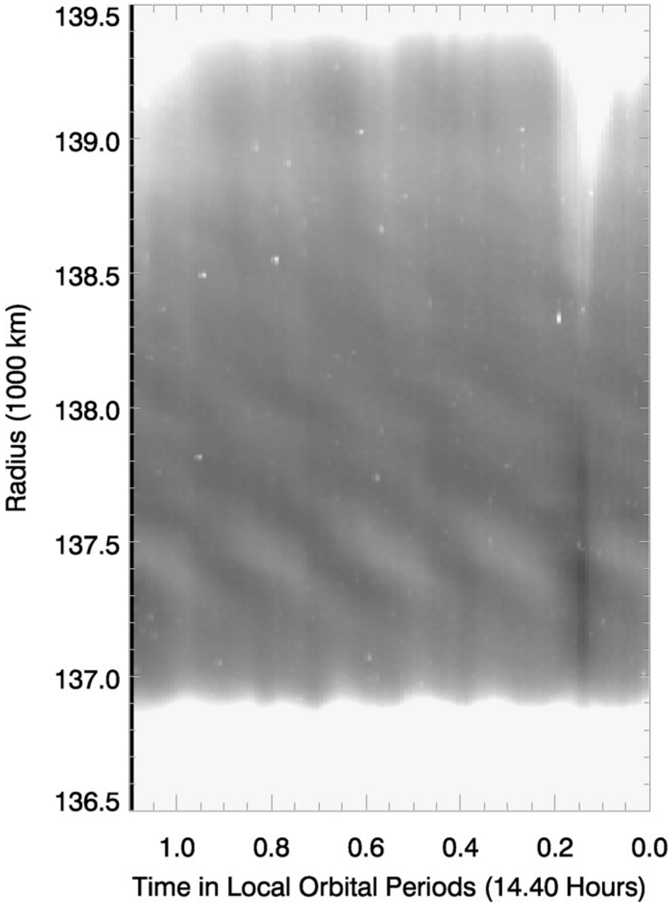

Fig. 2. Map of the Roche Division derived from the Rev 36 sequence, showing the brightness of this ring at an inertial longitude of ∼288° versus radius and time. Vertical bands near the top of this image correspond to features in the F ring (Murray et al., 2008). The wavy edge near the bottom of the image is the non-circular outer edge of the A ring (Spitale et al., 2008). Longitudinal brightness variations can be clearly seen between 137,000 and 138,200 km. Note that an average background level is subtracted from each radial scan to make this image. Similar maps of this region derived from the other data sets are given in Appendix A (Figs. 21–26).

maps display the brightness of the ring at the longitude observed by the cameras as a function of radius and time. Such maps are generated by simply stacking the radial scans together to form a two-dimensional array, and they have the advantage that they present the data without any assumptions regarding the speed at which the patterns move around Saturn. A constant background level (Roche Division) or linear trend with radius (D ring) is removed from each scan prior to making these maps. Note that time increases to the left in these plots. This ensures that the observed structures have the same orientation as they do in subsequent plots of brightness versus radius and (co-rotating) longitude.

These maps clearly reveal azimuthal brightness variations in both the D ring and the Roche Division. The D ring contains two zones of azimuthally variable structures, one extending inward from 73,000 km to approximately 72,000 km from Saturn's center, and a second centered around 71,500 km. The former region lies just interior to the D73 ringlet, while the latter corresponds roughly to the D72 ringlet as observed by Cassini (Hedman et al., 2007a). In the Roche Division, azimuthally variable features can be observed from near the edge of the A ring at 136,800 km out to approximately 138,500 km. Note that while there is little evidence for azimuthally periodic structures in the D ring, the structures in the Roche Division are clearly periodic, with four features moving through the observed longitude during the course of one local orbital period.

The procedures used to reduce the G ring data from Rev 29 are somewhat different from those used with the other data sets. These images captured a sufficiently broad range of longitudes that azimuthal brightness variations could be observed within a single image. Consequently, radial scans of entire images are unable to adequately resolve the structures of interest here. Instead, we computed the radius and longitude in the ring plane for each pixel in all of the images. Then, assuming a particular pattern speed, we binned the brightness measurements as functions of radius and co-moving longitude to produce the map shown in Fig. 3. Note that while this procedure requires assuming a pattern speed for the structures of interest, this is not a major problem because the G-ring features are narrowly confined in radius and there are reasonable candidates for the pattern speed (see below). The specific structures under consideration here are the series of dark gashes seen around 170,000 km, which lie well outside the bright arc at 167,500 km described in Hedman et al. (2007b).

2. The G-ring pattern and Lindblad resonances in faint rings

Despite the differences in the detailed morphology of the patterns in these three regions, they can all be interpreted as the result of perturbations to particle orbits by Lindblad resonances. The following section develops a model that relates the brightness variations in these regions to the relevant resonant perturbations. This analysis uses the pattern observed in the G ring as an archetype of these structures not only because it has the simplest structure, but also because the pattern's location and symmetry properties securely connect it to a specific resonance with a known satellite. Having used the G-ring data to clarify the connections between Lindblad resonances and patterns in faint rings, we will then investigate the more complex patterns observed in the D ring and Roche Division.

2.1. The dynamics of Lindblad resonances

Lindblad resonances, originally considered in galactic dynamics, have been discussed extensively in the context of Saturn's rings because they are responsible for generating the density waves observed in the main rings, especially the A ring (see, for example, Goldreich and Tremaine, 1982; Shu, 1984; Tiscareno et al., 2007; and references therein). However, the structures discussed here occur in a qualitatively different environment from those that produce density waves. Density waves occur in rings with sufficient mass and optical depth that the rings' surface mass density and collisions between particles are important. By contrast, the rings considered here have low optical depths, so interparticle collisions and disk self-gravity should be negligible. At the same time, most of the visible particles in these rings are less than 100 μm across, so non-gravitational processes such as plasma drag and radiation pressure, which are negligible in the main rings, probably play an important role. It is therefore worthwhile to review the basic dynamics of Lindblad resonances.

Consider a planet with a single satellite on a circular orbit, and let us investigate the orbit of a test particle in an equatorial, eccentric orbit around the planet. For the moment, we will neglect any possible non-gravitational forces. Say the longitudes of the particle and the satellite are λ and λ_s, respectively, and the longitude of pericenter for the test particle's orbit is ϖ. The condition for a first-order Lindblad resonance is that the quantity (known as the resonant argument):

$$\varphi = j(\lambda - \lambda_s) - (\lambda - \varpi) \tag{1}$$

is constant in time for some integer value of j, with positive (negative) values of j corresponding to the perturber orbiting exterior (interior) to the test particle.

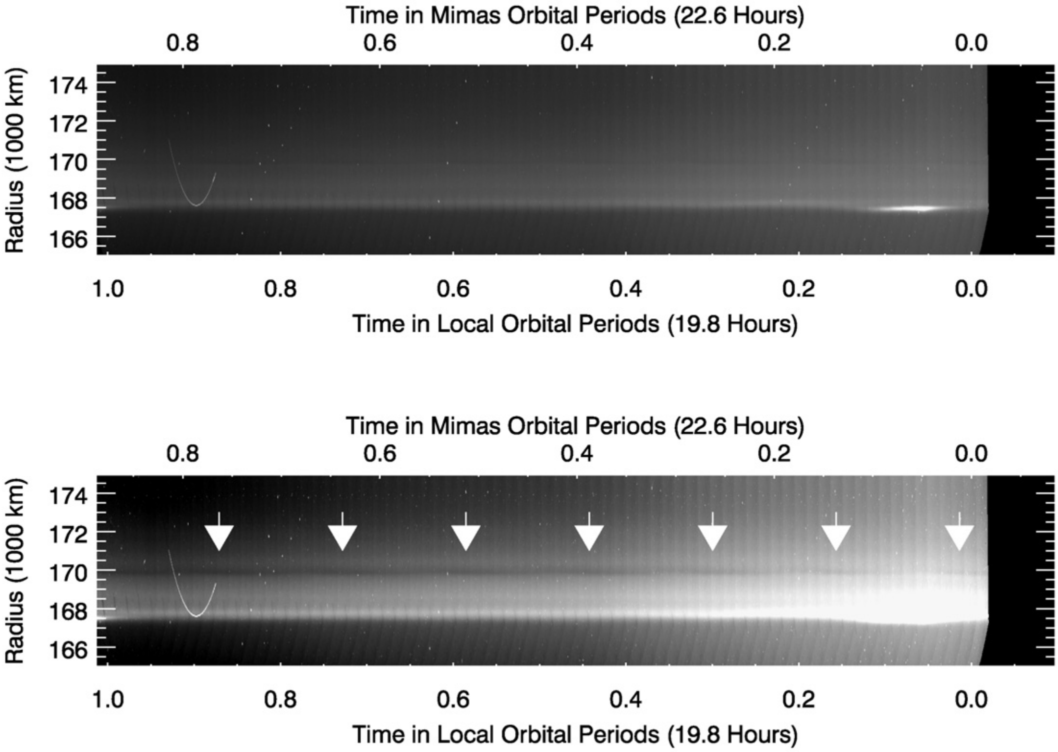

Fig. 3. Maps of the G ring derived from the Rev 29 imaging data, showing the ring's brightness at an inertial longitude of ~298° as a function of radius and time. The top panel shows the arc in the G ring (discussed in Hedman et al., 2007b) at a radius of 167,500 km and a time between 0.05 and 0.15 local orbital periods. The bottom panel is stretched to highlight faint features. The vertical bands correspond to the edges of the individual images from which this map was generated. The bright arc near the left edge of the image is a camera artifact in one image. The white arrows highlight a series of dark streaks that can be associated with the 8:7 ILR with Mimas. Fig. 5 provides a higher-resolution view of these structures.

Note that $\lambda - \lambda_s = 0$ corresponds to a conjunction between the satellite and the ring particle, and that $\lambda - \varpi$ measures the true anomaly, i.e., how far the particle is from pericenter. The condition that φ is constant therefore means that if the particle starts at periapse during one conjunction (i.e., $\lambda - \varpi = 0$ when $\lambda - \lambda_s = 0$), then by the next conjunction it will be back at periapse again (i.e., $\lambda - \varpi = 2\pi j$ when $\lambda - \lambda_s = 2\pi$). This means the test particle is always at the same phase in its eccentric orbit when it passes longitudinally close to the satellite, so perturbations from the satellite can build up to strongly influence the eccentricity and pericenter locations of particle orbits near such resonances.

In other words, the satellite's perturbations break the rotational symmetry of the problem. Without the perturber, a particle with any eccentricity and any orientation will maintain the same eccentricity and steadily precess around the planet. With the perturber, only certain orbits maintain a constant eccentricity (for more details, see Murray and Dermott, 1999, especially Chapter 8). These "stable" orbits can be depicted as "streamlines" that have a relatively simple form in the reference frame of the perturbing object. Fig. 4 shows a cartoon of streamlines for the case where $j = 8$, also called an 8:7 Inner Lindblad Resonance (8:7 ILR). The streamline orbits form closed eight-lobed figures in the moon's reference frame. Furthermore, these paths maintain a particular orientation with the perturbing satellite. This simply indicates that the orbits with stable eccentricities are always at pericenter (apocenter) during conjunction if they are inside (outside) the exact resonance location. In general, a $j : j-1$ Lindblad resonance will have streamlines forming a j-lobed figure in a frame co-rotating with the perturber.

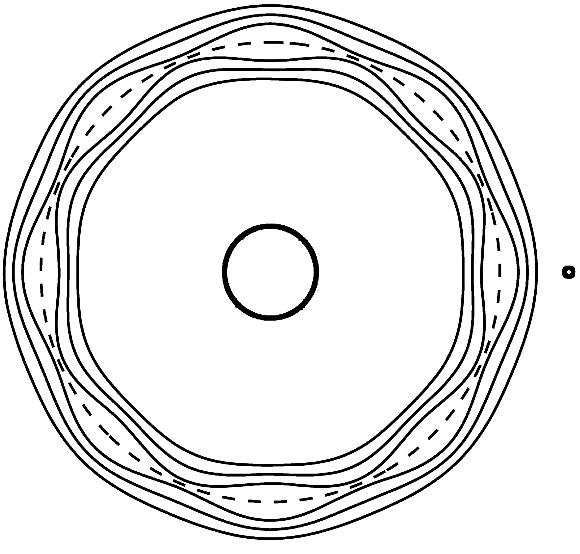

Fig. 4. Cartoon of a classical 8:7 resonance as viewed from the reference frame of the exterior perturbing satellite (shown as a spot on the right side of the plot). Note this image is not to scale. The dashed line marks the location of the exact resonance and the solid curves are "streamlines" of ring particles in the vicinity of the resonance. Note that streamlines closer to the exact resonance are not drawn for clarity, but could be populated in an optically thin ring.

To be a bit more quantitative, Eq. (10.22) in Murray and Dermott (1999) gives the expected forced eccentricity e_F for a particle whose orbit has a semi-major axis a near a first-order Lindblad resonance at semi-major axis a_r:

$$ae_F = \frac{\beta}{|\delta a|}, \tag{2}$$

where $\delta a = a - a_r$ and β is a measure of the resonance strength that depends on the mass of the perturber and the character of the resonance:

$$\beta \simeq \frac{a_r^2}{3}\frac{m}{M}\frac{2\alpha|f_d|}{(j-1)}, \tag{3}$$

where m/M is the ratio of the satellite's mass to the primary's mass, α is the ratio of the particle's and moon's semi-major axes and f_d is a constant associated with the particular resonance. It turns out that $2\alpha|f_d|/(j-1) \simeq 1.6$ for most first-order Lindblad resonances (Murray and Dermott, 1999, Fig. 10.10). Thus, if we assume that all the particles in the vicinity of the resonance have zero free eccentricity so that the eccentricity is that forced by the resonance, then all the particles with a given semi-major axis a will follow a streamline path in the co-rotating frame defined by the equation:

$$r = a + \frac{\beta}{\delta a}\cos\phi, \tag{4}$$

where r is the radial distance of the particle from Saturn's center and ϕ is a longitudinal phase measured relative to the perturbing moon (not to be confused with the resonant argument φ). For a $j : j-1$ resonance, $\phi = j(\lambda - \lambda_{\mathrm{moon}})$. Note that the amplitude of the radial excursions grows as the particle's semi-major axis approaches that of the exact resonance.

In practice, we do not observe the orbits of individual particles, but instead the local brightness of the ring material, which is directly proportional to the ring's local surface density if the optical depth is sufficiently low. Assume that the particles are evenly distributed in semi-major axis and also assume that the eccentricities are sufficiently small that density variations in longitudinal phase can be neglected. The phase-space number density $\rho(a,\phi) = \bar\rho$ will then be a constant. Then the observed density of particles as a function of radius and phase is given by (assuming streamlines do not cross, see Section 2.3):

$$\rho(r,\phi) = \frac{\bar\rho}{dr/da}. \tag{5}$$

In other words, the observed density scales inversely with the spacing between streamlines. Note that if the particles have free eccentricities, the density variations will still increase as the distance between streamlines decreases so long as the pericenter longitudes of the free components of their eccentricities are randomly distributed.

Since the stable orbits have a particular orientation relative to the perturbing satellite, the perturbations associated with the resonance will produce patterns in the surface density of the ring with j-fold rotational symmetry in a frame co-rotating with the satellite. Therefore, in spite of the fact that individual particles move at the local Keplerian rate, the pattern as a whole moves with the perturber. Differentiating Eq. (1), we find the speed of the pattern (which equals the mean motion of the perturber) is given by:

$$\Omega_p = \frac{(j-1)n + \dot\varpi}{j}, \tag{6}$$

where $n = d\lambda/dt$ is the local orbital mean motion and $\dot\varpi$ is the local orbital precession rate, both of which are determined by the planet's gravitational field. Note that since $\Omega_p = d\lambda_s/dt$ is also the mean-motion of the perturbing object, if we find a pattern in the rings that we suspect is due to a first-order Lindblad resonance with a given j, we can estimate the perturber's mean motion and orbital period. However, one has to exercise caution when identifying the symmetry of a pattern due to a resonance. Most of the data described above was obtained by staring at a particular inertial longitude in the ring plane and watching material move through the camera's field of view. Since in general $n \gg \dot\varpi$, the pattern speed of a Lindblad resonance $\Omega_p \simeq \frac{j-1}{j}n$. Thus, in one local orbital period, where we would see the full 360° of a pattern rotating at the local orbital rate move through the field of view, we would only see $360°(j-1)/j$ of the resonantly generated pattern. The j-fold symmetric pattern produced by the resonance can therefore look like a $(j-1)$-fold symmetric pattern moving at the local Keplerian rate.

Classical Lindblad resonances occur when the periodic forcing on a particle from a nearby satellite matches the particle's epicyclic oscillation rate. However, similar periodic forcings can also occur with axially asymmetric density variations in the planet's interior (Marley and Porco, 1993) and with periodic electromagnetic forces, in which case they have been called Lorentz resonances (Burns et al., 1985). The associated particle dynamics of all such resonances mimic those of Lindblad resonances (Hamilton, 1994) and so we use "Lindblad resonance" here as a generic term for any situation where a periodic forcing is commensurate with the particle's eccentric epicyclic motion, regardless of the nature of the perturbing force. Furthermore, we distinguish generic "Inner Lindblad Resonances" (or ILRs) from generic "Outer Lindblad Resonances" (or OLRs) by stipulating that for ILRs the perturbation period is longer than the local orbital period (i.e., $j > 0$ in the above expressions), while for OLRs the perturbation period is shorter than the local orbital period (i.e., $j < 0$). Note that with this convention, Inner Lindblad Resonances all lie *inside* the semi-major axis that co-rotates with the perturbing force and the Outer Lindblad Resonances all lie *outside* this semi-major axis. This means that for classical Lindblad resonances with satellites, Inner (Outer) Lindblad Resonances lie interior (exterior) to the perturbing satellite's orbit, while for resonances with the planet's interior or magnetic field, the Inner (Outer) Lindblad Resonances occur interior (exterior) to the synchronous orbit.

2.2. The G ring structure and the 8:7 Mi ILR

At this point, it is useful to take a closer look at the clearest example of a pattern in a faint ring generated by a Lindblad resonance: the series of dark streaks in the outer G ring at a radius of 169,800 km from Saturn's center (see Fig. 3). This pattern straddles the predicted location of the $j = 8$ Inner Lindblad Resonance with Saturn's moon Mimas (also known as the 8:7 Mi ILR). If this resonance were responsible for this pattern, then we would expect an 8-fold symmetric pattern rotating at the same speed as Mimas. Since Mimas' orbital speed is 7/8 the local Keplerian orbital speed of a G-ring particle, the $j = 8$ pattern produced by Mimas will move at 7/8 the local orbital rate. Indeed, we find that eight dark streaks moved through the field of view during one orbital period of Mimas, or seven moved through during one local orbital period (see Fig. 3). The symmetry properties are therefore consistent with what one would expect to be associated with the 8:7 ILR.

Further evidence that this pattern is created by a resonance is presented in Fig. 5, where the brightness variations are normalized relative to the mean brightness level and are binned in radius and a parameter that we call the "phase":

$$\phi = 8\cdot(\lambda - \lambda_{\mathrm{Mimas}}) \bmod 360°. \tag{7}$$

Note that zero phase corresponds to a longitude aligned with the moon. Binning the data in terms of this parameter co-adds the pixels from multiple streaks together, improving the signal to noise, which enables us to verify that the brightness variations are indeed strongest near the location of the exact resonance. Furthermore, we find the pattern's brightness minima are aligned with Mimas. This is consistent with the cartoon of these resonances shown in Fig. 4, where the streamlines are organized such that particles avoid the region closest to the resonance near conjunction with the satellite. The basic pattern observed at this region therefore makes sense as the result of perturbations from the 8:7 ILR.

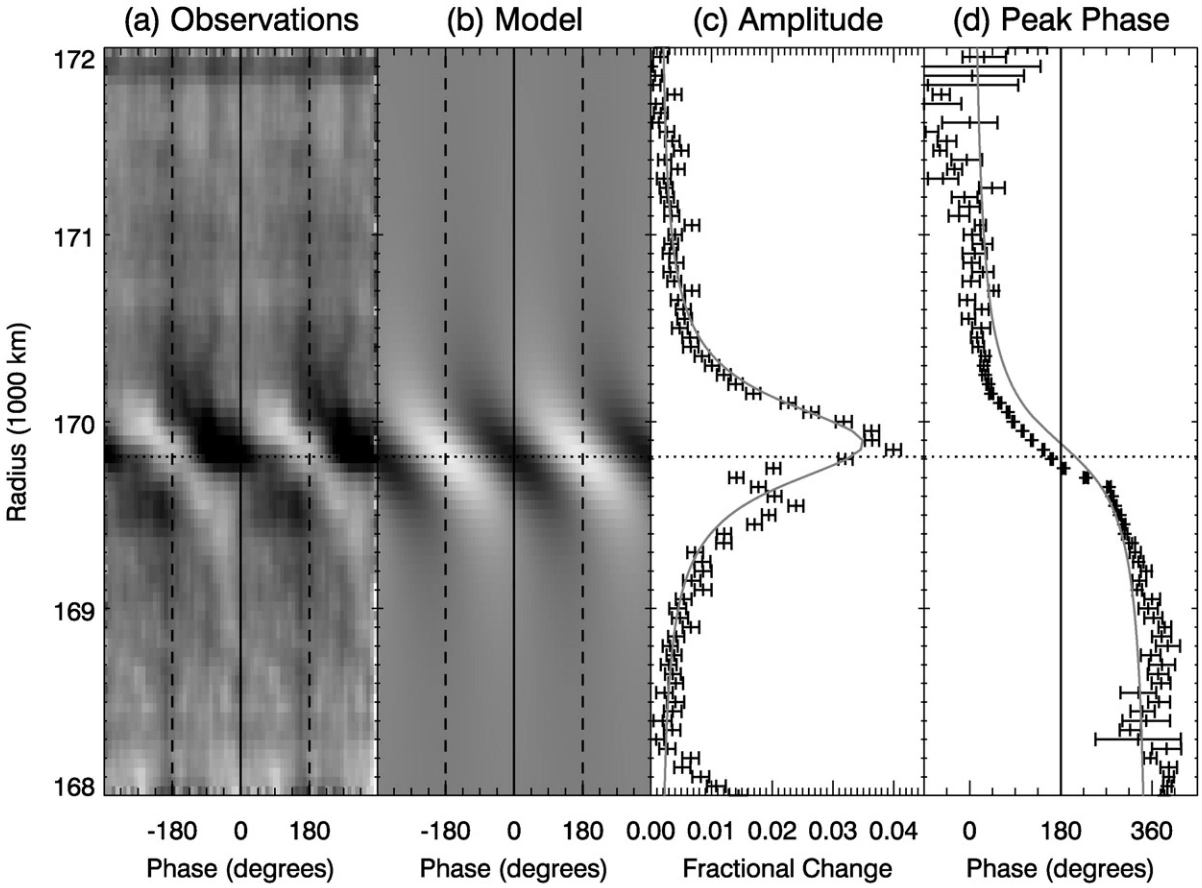

Fig. 5. A closer look at the 8:7 Mimas ILR in the G ring. Panel (a) is an image showing the background-subtracted brightness of the G ring as a function of radius and pattern phase $\phi = 8 \cdot (\lambda - \lambda_{\text{Mimas}})$. $\phi = 0°$ therefore corresponds to a longitude in conjunction with Mimas (the same data are shown twice for clarity). Panel (b) shows a simple model of the brightness variations described in the text. Panels (c) and (d) show the normalized amplitude and phase of the azimuthal brightness variations as a function of radius. The brightness asymmetry peaks at the exact resonance location, while the phase of the pattern varies systematically with radius. The amplitude data are fit to the model described in the text. The curves show the best-fit model predictions for both the amplitude and the phase, which match the observed data reasonably well. The horizontal dotted line marks the predicted location of the exact resonance.

One unexpected aspect of the pattern revealed in Fig. 5 is that the alternating bright and dark streaks produced by this resonance are canted relative to the radial direction. This is difficult to explain in terms of a simple picture like Fig. 4, which suggests that the density perturbations would be symmetric about the $\phi = 0$ line. In the following section, we develop a relatively simple model that succeeds in reproducing the morphology of this resonance and therefore provides a useful way to describe these structures.

2.3. A model for Lindblad resonances in faint rings

Recall that the ring's local surface density is related to the distance between streamlines and is given by:

$$\rho(r, \phi) = \frac{\bar{\rho}}{dr/da}. \tag{8}$$

Strictly speaking, this equation only applies if streamlines do not cross, i.e., dr/da never equals zero. Fortunately, this condition seems to apply to all of the structures discussed here.

The observed brightness variations associated with the patterns seen in all of the rings are everywhere less than 10% of the mean brightness (note that since these features are multiple pixels across, the camera's finite resolution should not significantly reduce the contrast in this case). Such subtle variations are inconsistent with any streamline-crossing, which necessarily produce large (greater than order unity) fractional brightness variations. Thus the eccentricities forced by the resonance only cause small perturbations to the local density. In other words, $dr/da = 1 - y$ with $y \ll 1$ everywhere and the fractional density variations are given approximately by:

$$\delta\rho(r, \phi) = \frac{\rho(r, \phi) - \bar{\rho}}{\bar{\rho}} \simeq 1 - \frac{dr}{da}. \tag{9}$$

If we follow the "classical" treatment of Lindblad resonances, discussed above, then the streamline paths are defined by:

$$r = a + \frac{\beta}{\delta a} \cos\phi, \tag{10}$$

where r is the particle's radial distance from Saturn center and ϕ is its longitudinal phase measured relative to the perturbing moon. For a $j : j - 1$ resonance, $\phi = j(\lambda - \lambda_{\text{moon}})$, where λ and λ_{moon} are the longitudes of the particle and the moon, respectively.

Differentiating Eq. (10), we find:

$$\frac{dr}{da} = 1 - \frac{\beta}{(\delta a)^2} \cos\phi. \tag{11}$$

The density variations in this case are therefore given by:

$$\delta\rho(r, \phi) = \frac{\beta}{(\delta a)^2} \cos\phi, \tag{12}$$

which goes to infinity at the exact resonance. This singularity vanishes in the proper treatment of these resonances, where higher-order terms are included in the perturbation expansion, but the above simple expression is nearly correct where $\delta a^2 \gg \beta$. In this regime, $\delta\rho(r,\phi) \propto \cos\phi$ for all r. This means that the density maxima and minima occur at the same phase for all radii, so any bright and dark streaks would be purely radial. This model therefore cannot account for the tilted nature of the streaks observed around the 8:7 ILR (Fig. 5). Including higher-order perturbation terms does not alter the phase of the radial excursions and therefore cannot produce a tilt in the brightness variations. However, the alignment of streamlines can be altered by introducing some form of dissipation into the system (Hañninen and Salo, 1992; Wada, 1994). Thus, to explain the observed patterns, we use a simple phenomenological model of the resonance dynamics to insert a dissipative term into the equations of motion.

The dynamics of any Lindblad resonance can be grossly approximated with that of a driven harmonic oscillator. Say we have a particle on an orbit with semi-major axis a and mean-motion n which is near the mean motion of the exact resonance n_r, then the equation of motion for the particle's radial excursions $x = r - a$ can be approximately written as:

$$\frac{d^2x}{dt^2} = -n^2x - B\cos(n_r t), \tag{13}$$

where B is the strength of the driving term and the sign on this term is selected so the solution matches the above findings. One can quickly convince oneself that the solution to this equation of motion is:

$$x = \frac{B}{n_r^2 - n^2}\cos(n_r t). \tag{14}$$

Note that $n_r t$ is the same as the phase parameter ϕ defined above. Furthermore, since $n^2 = GM/a^3$ (where M is Saturn's mass), near the resonance we can approximate:

$$n_r^2 - n^2 \simeq \frac{3GM}{a_r^4}\delta a, \tag{15}$$

to obtain:

$$x = r - a = \frac{\beta}{\delta a}\cos\phi, \tag{16}$$

where $\beta = B\cdot(3GM/a_r^4)^{-1}$, which matches Eq. (10).

Now let us add a damping term into this equation of motion:

$$\frac{d^2x}{dt^2} = -n^2x - \frac{1}{\tau}\frac{dx}{dt} - B\cos(n_r t), \tag{17}$$

where τ is the effective damping time for radial excursions (i.e., eccentricities). The steady-state solution to this equation has the familiar form (see, for example, Baierlein, 1983):

$$x = x_o\cos(n_r t + \phi_o), \tag{18}$$

where

$$x_o = \frac{B}{[(n_r^2 - n^2)^2 + (n_r/\tau)^2]^{1/2}} \tag{19}$$

and

$$\tan\phi_o = \frac{n_r/\tau}{n_r^2 - n^2}. \tag{20}$$

Again, it is useful to change variables from mean motion to semi-major axis, in which case:

$$x_o = \frac{\beta}{[(\delta a)^2 + L^2]^{1/2}} \tag{21}$$

and

$$\tan\phi_o = \frac{L}{\delta a}, \tag{22}$$

where $L = a_r/(3n_r\tau)$ is a "damping length" and β is the same parameter as in the undamped case (cf. Eq. (10)).

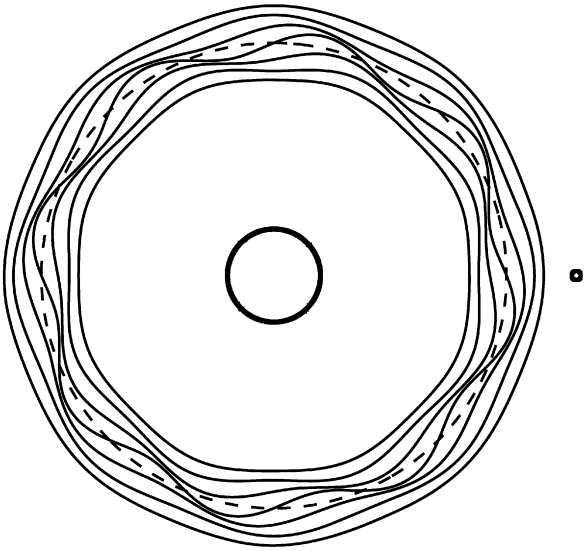

Fig. 6. Cartoon of a "damped" 8:7 resonance as viewed from the reference frame of the perturbing satellite (compare with Fig. 4). Again, the dashed line marks the location of the exact resonance and the solid lines are "streamlines" of ring particles in the vicinity of the resonance. The finite damping term in the equation of motion causes the phase of these orbits to change continuously across the resonance.

The equation for the streamlines is then:

$$\begin{aligned} r &= a + x = a + x_o\cos(\phi + \phi_o) \\ &= a + x_o(\cos\phi\cos\phi_o - \sin\phi\sin\phi_o) \end{aligned} \tag{23}$$

or

$$r = a + \frac{\beta}{[(\delta a)^2 + L^2]}(\delta a\cos\phi - L\sin\phi). \tag{24}$$

Fig. 6 illustrates the shape of the streamlines in this situation. Note that there is no longer an abrupt transition at the exact resonance. Instead, the locations of the particle orbits' apocenters change gradually across the resonance.

When we differentiate this equation with respect to a, we get:

$$\frac{dr}{da} = 1 - \frac{\beta}{[(\delta a)^2 + L^2]^2}\left[\left((\delta a)^2 - L^2\right)\cos\phi + 2\delta a L\sin\phi\right]. \tag{25}$$

We can already observe that so long as $\beta/L^2 \ll 1$, then $dr/da - 1$ will be small everywhere, even at the exact resonance. In this limit, the normalized density variations will be:

$$\delta\rho(r,\phi) = \frac{\beta}{[(\delta r)^2 + L^2]^2}\left[\left((\delta r)^2 - L^2\right)\cos\phi + 2\delta r L\sin\phi\right]. \tag{26}$$

We therefore get a sinusoidal density variation at each radius r with an amplitude A given by:

$$A(r) = \frac{\beta}{(\delta r)^2 + L^2} \tag{27}$$

and a phase θ given by:

$$\tan\theta(r) = \frac{2\delta r L}{(\delta r)^2 - L^2}. \tag{28}$$

Figs. 5c and 5d show the measured values of $A(r)$ and $\theta(r)$ for the observed data, together with a model fit to $A(r)$ of the above form. This fit gives a damping length $L \simeq 280$ km and a peak amplitude of about 0.033, which corresponds to a $\beta \simeq 2500$ km^2. If we use these parameters in Eq. (26), we can produce a model of the brightness variations that matches the observed data fairly well in both amplitude and radial extent (see Fig. 5b). We may also note that the expected phase of the pattern matches the observed phase reasonably well (Fig. 5d).

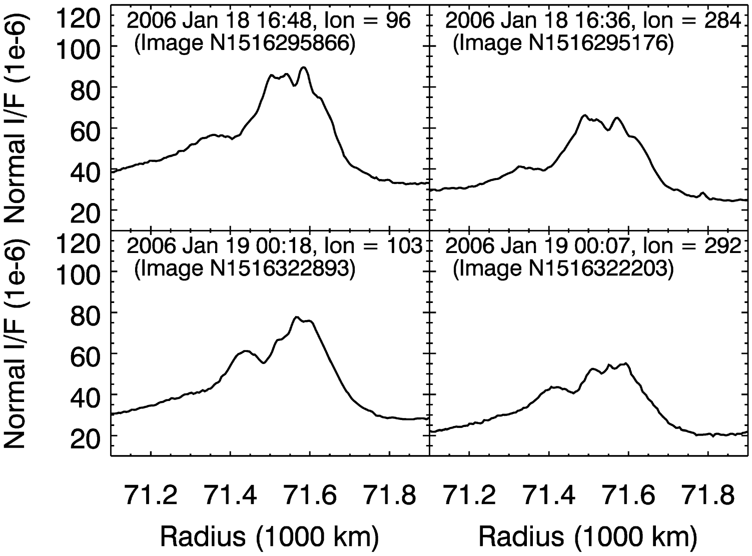

Fig. 7. Radial brightness profiles of the region around the D72 ringlet. Each row shows profiles of both ansae of the rings taken at nearly the same time. The top pair of images were taken only 8 hours before the bottom pair of images. Both of the top profiles show a notch at 71,400 km. In the lower profiles the notch has shifted at both ansae to around 71,500 km. Similar shifts can be seen in the structure around 71,600 km. See also Fig. 8.

The damping length of 280 km corresponds to a damping time $\tau = a_r/3n_rL$ of approximately one month. This is a rather short time scale and corresponds to strongly damped eccentricities. However, the above model is generic and therefore does not specify the physical mechanism responsible for the dissipation. Further discussion of possible dissipative processes is given in Section 5 below, where the properties of the structures observed in all of the different faint rings can be compared.

The β parameter, which measures the resonance's strength, should match predictions from perturbation theory. According to Murray and Dermott (1999, Eq. (10.22)) (Eq. (3) above):

$$\beta \simeq \frac{a_r^2}{3}\frac{m}{M}\frac{2\alpha|f_d|}{(j-1)}, \tag{29}$$

where a_r is the semi-major axis (~170,000 km), m/M is the ratio of the mass of the perturber (Mimas) to the mass of the primary ($\sim 6.6 \times 10^{-8}$), and the remaining factors depend on the resonance, but $2\alpha|f_d|/(j-1) \simeq 1.6$ for most first-order Lindblad resonances (Murray and Dermott, 1999, Fig. 10.10). Thus for the 8:7 Mi ILR, $\beta \simeq 1000\ \text{km}^2$. This is a factor of two lower than the value of β that best fits the observations, but given that this is a purely phenomenological model, this degree of agreement is encouraging.

3. Identification of resonant structures in the D ring and the Roche Division

While the above model is based on a single example of a Lindblad resonance in a faint ring and certain aspects of the physics (in particular, the nature of the damping term) are not fully understood, the basic dynamics involved are sufficiently generic that we should be able to use this model with other faint rings to identify additional examples of Lindblad resonances in faint rings. Specifically, the considerations presented in the previous section allow us to identify a series of 2:1 Inner Lindblad Resonances in the D ring and 3:4 Outer Lindblad Resonances in the Roche Division.

3.1. Evidence of 2:1 Inner Lindblad Resonances in the D ring

A complex assortment of anastomosing bright and dark diagonal streaks is observed throughout the middle D ring between 71,000 and 73,000 km (see Fig. 1 and also Appendix A). These patterns are much more complex than the simple alternating streaks seen in the G ring, and the patterns do not repeat in less than one local orbital period, so it is not immediately apparent that resonances play a role in producing these structures. Indeed, these structures at first appear to be much like the "jets" or "spirals" in the F ring, i.e., transient phenomena produced when a localized brightness enhancement evolves due to Kepler shear (Charnoz et al., 2005; Murray et al., 2008). However, certain characteristics of these structures indicate that they are patterns imposed on the ring material by periodic perturbing forces analogous to those operating in the G ring (cf. Burns et al., 1985).

If these structures were transient phenomena produced by Kepler shear, then we would expect the radial wavelength of the pattern to steadily decrease over time. Given this structure's proximity to the planet, any longitudinally localized density enhancement will shear out to become a smooth band in only a few weeks. In fact, the typical radial wavelength of the pattern around 71,500 km (D72) in all of these sequences is around is 50 km, which is not substantially different from the wavelengths observed in high-resolution images obtained in 2005 (Hedman et al., 2007a). This strongly suggests that these structures are persistent features of these rings, and implies that these patterns are imposed on this material by outside forces.

Another important clue to the origin of these structures comes from images taken in early 2006 and previously described in Hedman et al. (2007a). These observations include several pairs of images covering both ansae of the D ring (separated by 180° in longitude) at nearly the same time. Radial brightness profiles derived from these images are provided in Figs. 7 and 8 (compare with Fig. 12 in Hedman et al., 2007a). For any pair of images taken at the same time, the radial structure of the ring at one ansa is nearly identical to the structure on the other ansa. Furthermore, the structures seen at both ansae change in the same manner over the course of eight hours.

The striking symmetries between the two ansae can be explained if the structures observed in this part of the D ring are in fact periodic patterns generated by 2:1 Inner Lindblad Resonances, that is, Lindblad resonances with $j = 2$. The pattern imposed on a ring by such a resonance will have 2-fold symmetry, with the same structure at two opposite sides of the ring (this is the $j = 2$ analog of the symmetry pattern drawn in Fig. 4). This is consistent with the profiles shown in Figs. 7 and 8. Furthermore, in this situation

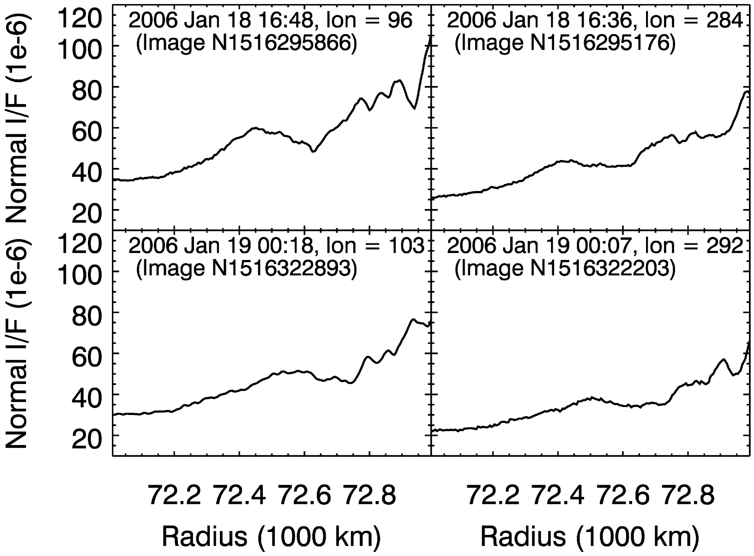

Fig. 8. Same as Fig. 7, but for the region interior to D73. Here the prominent dip shifts from 72,600 km to 72,700 km.

the perturbation period is roughly twice the local orbital period, so the pattern rotates around Saturn at approximately half the local orbital rate, and only one-half of the complete pattern will move through the observed longitude in one local orbital period. This is consistent with the 2007 data, which do not yield repeating patterns moving through a fixed inertial longitude in less than one local orbital period.

Even so, the structures in the D ring cannot be attributed to a single 2:1 ILR. The patterns seen in this ring are much more extensive and complex than the feature visible in the G ring. Furthermore, the details of the pattern change over time (compare Fig. 1 with the D-ring maps in Appendix A), so the entire structure cannot be moving at a single rate. Instead, it appears that multiple discrete sub-patterns are present and that they are drifting past each other over the course of the observation. Fig. 9 shows a close-up of one of these sub-patterns centered at 71,600 km. This individual structure consists of diagonal dark and bright streaks, much like the pattern seen in the G ring. The pattern is also fairly stable, not changing much during the course of the 100 days between Rev 37 and Rev 43. Furthermore, when all the scans are projected onto a longitude system that is co-rotating with the predicted pattern speed of a 2:1 ILR at this radius, the different scans show the bright features at the same locations, which demonstrates that this pattern does move at a rate consistent with a 2:1 ILR. (However, we caution that the present data are insufficient to uniquely determine the mean motion of the pattern, so other solutions are possible.) Thus we interpret these structures in the D ring to represent a *cluster* of distinct 2:1 ILR patterns with a range of pattern speeds. As these patterns drift past each other, the details of the structure change, but the persistence of the sub-patterns insures that the overall character of the structures remains roughly the same.

We will discuss the range of pattern speeds associated with these structures in detail in Section 4.2. However, a range of pattern speeds implies a family of perturbers with similar but not identical periods. This is *not* what we would expect from satellites, since they would produce single features like the one visible in the G ring. Furthermore, the range of pattern speeds in this ring corresponds to periods between 10.5 and 10.9 hours, which does not match any known satellite's orbital period but is close to rotation periods associated with Saturn's winds and magnetic field.

3.2. Evidence for a 3:4 OLR in the Roche Division

The periodic patterns in the Roche Division occur near the orbit of Atlas, at roughly 137,500 km from Saturn's center, where a concentration of material was noted by Porco et al. (2005a). The maps of this region revealed that this was not a simple ringlet, but a much more complex structure consisting of alternating bright and dark streaks (see Fig. 2 and Appendix A). Unlike the structures in the D ring, the patterns here are clearly periodic, with four bright (or dark) streaks moving through the observed longitude in one local orbital period. Furthermore, comparisons of data from the multiple observations of this region reveal that these patterns do not move around Saturn at the local orbital rate.

Fig. 10 shows maps of a portion of the Roche Division derived from the two observations obtained during Rev 29. The data for both have been projected into a longitude system co-rotating at the local mean motion (orbital period = 14.4 hours). Bright and dark features clearly do not line up well in these two sequences, and since the two sequences are only separated in time by a day or two, the pattern speed must be very different than the local orbital speed.

The symmetry properties of the pattern can help narrow down the possible speeds associated with these patterns. Since four bright features move through the field of view during one local orbital period, this pattern could be a 5:4 ILR with a corresponding perturbation period of approximately 18 hours. Alternatively, the pattern could be a 3:4 Outer Lindblad Resonance with $j = -3$ and a 3-fold symmetric pattern moving at 4/3 the local orbital speed. In this case, the period of the structure would be around 10.8 hours, close to the same period as some of the structures in the D ring. Using a co-rotating longitude system with a period of approximately 10.8 hours produces maps where the bright and dark features are much better aligned (see Fig. 11, also Fig. 12). At present, we cannot definitively rule out the possibility that this structure is due to a 5:4 ILR. However, the similarity of the 3:4 OLR pattern speed to the 2:1 ILR pattern speeds in the D ring is suggestive.

If we compare the parts of the D ring and the Roche Division that should have the same pattern speeds, we find that the similarities between these two patterns are very strong indeed. Figs. 12 and 13 show maps of portions of the Roche Division and D-ring which should have the same pattern speeds, plotted using a common co-rotating longitude system with a pattern speed of 10.82

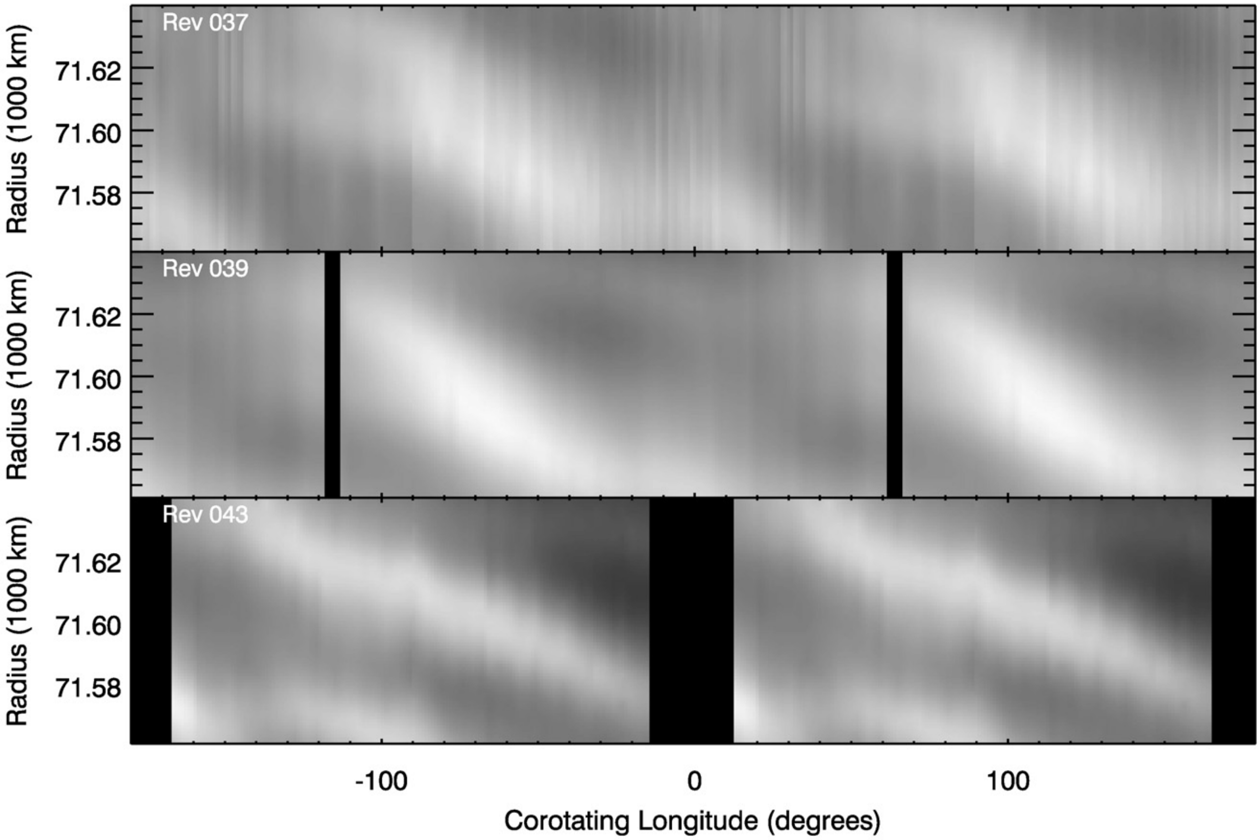

Fig. 9. A close-up of part of the structure in the D ring near the peak of the D72 ringlet. The data from the different sequences are all precessed to the same co-rotating longitude system with a mean motion corresponding to the 2:1 ILR pattern speed at this radius (period = 10.56 hours). The same data are repeated twice in each map for clarity of presentation. All images contain a series of bright and dark tilted streaks similar to those observed in the G ring (see Fig. 5). Note that the brightness maxima in the different scans occur at the same phase in this rotating coordinate system, which implies that this pattern rotates around the planet at a rate consistent with that expected for a 2:1 Lindblad resonance.

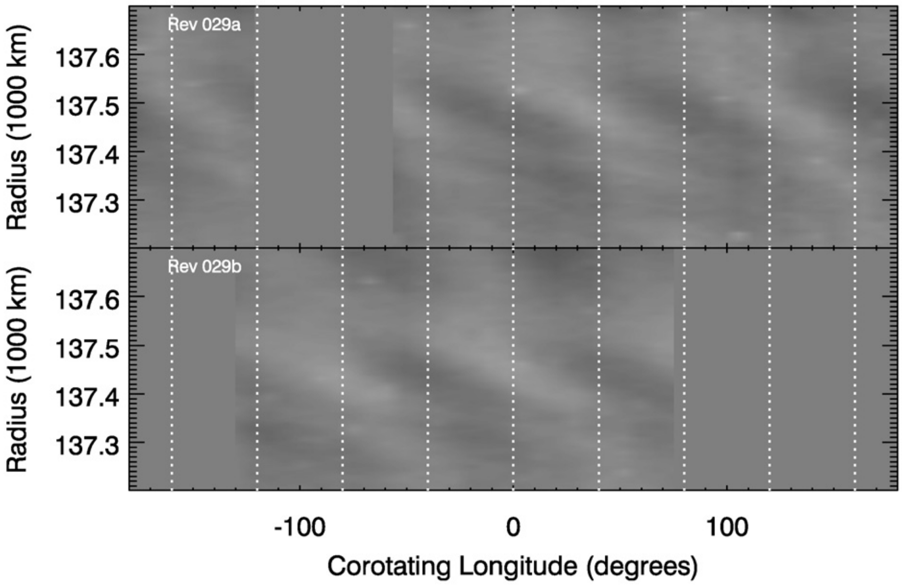

Fig. 10. Structures in the Roche Division observed during Rev 29, aligned assuming the local co-rotation speed (corresponding to an orbital period of 14.4 hours). Note the patterns in the two panels, taken only a day or so apart, do not line up. This implies the pattern speed is very different from the local corotation speed.

hours. In both cases we can observe the overall pattern evolve with time, possibly because various sub-patterns are drifting relative to each other as discussed above. Ideally, if these two sequences of observations were contemporaneous, we should be able to see similar patterns evolving in similar ways at similar times in these two regions. Unfortunately, the Roche Division sequences are all earlier than the D ring sequences, so we do not have truly contemporaneous observations to compare. Even so, the two sets of observations are sufficiently close in time that we can note some interesting trends.

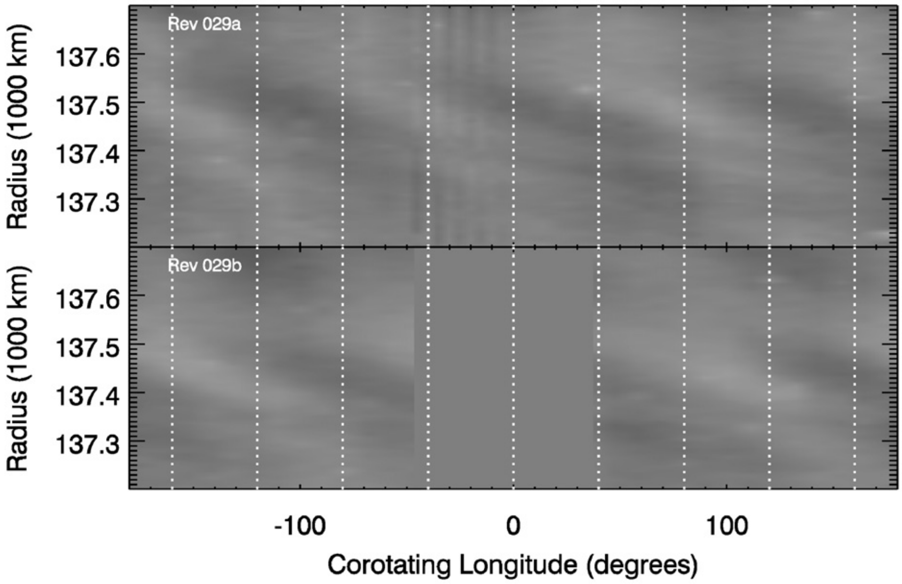

Fig. 11. The same data as shown in Fig. 10, now precessed using a pattern speed associated with the 3:4 outer Lindblad resonance (period = 10.8 hours). The bright and dark features are clearly better aligned than they are in the previous figure.

If we look at the Roche Division data, we observe that between Rev 29 and Rev 36 the pattern becomes more organized. In the earlier observations the most prominent structure is a series of narrow dark gashes near 137,600 km. In Revs 33 and 36 the pattern appears as a series of broad bright diagonal streaks with equally broad dark streaks between them. Again, we could attribute this change to be the result of several sub-patterns coming into alignment and producing a more dramatic overall pattern. Alternatively, the strength of the perturbations or the damping timescale may be changing over this time interval.

If we now turn to the D-ring data (Fig. 13), we notice that in Rev 37 the pattern here is also well organized, with broad dark and bright streaks extending over a relatively wide range of radii. By Rev 43, however, this structure has become less distinct, with the most prominent feature being a narrow dark gash near 72,700 km, much like the earliest Roche Division observations. Thus the changes over time in the Roche Division and the D ring are consistent in that they show a structure that first becomes more organized and then shears out again.

Further evidence that the patterns in the Roche Division are generated by resonances with a sub-set of the same perturbation periods as those found in the D ring will be presented below, where we study the possible perturbation periods in detail.

4. Quantifying the perturbations

The patterns in the D ring and Roche Division are both consistent with resonant structures generated by perturbation periods between 10.5 and 10.9 hours; this range overlaps the rotational periods associated with Saturn's winds and magnetosphere. To further investigate this suggestive coincidence in more detail, we will now explore various techniques to identify the strongest and most persistent perturbation periods operating in these regions.

4.1. Amplitudes of brightness variations

Our model of resonance-induced structures in faint rings indicates that the longitudinal brightness variations generated by a specific resonance reach a maximum at the location of the exact resonance, and the amplitude of the variations at the exact resonance is proportional to the strength of the resonance. Thus local maxima in the fractional longitudinal brightness variations in the D ring and the Roche Division should mark the locations of the strongest resonances in these regions.

For each imaging sequence, the amplitude of the brightness variations is computed by fitting the appropriate data versus phase to a sine curve. To convert these amplitudes into measurements of the fractional brightness variations, they must be normalized to the mean brightness of the ring material at the appropriate radius. However, the average brightness measured by the camera at a given radius may include spurious instrumental backgrounds, which must be removed to obtain a reasonably accurate measurement of the actual ring brightness. Visual inspection of the relevant images do not reveal obvious patterns due to stray light, so any instrumental background likely corresponds to a constant offset.

For the Roche Division data, the relevant images include regions outside the F ring, where the measured brightness is several times lower than the mean brightness between the A and F rings. This implies that instrumental backgrounds are not an issue for these data.

By contrast, the D ring images discussed here do not include the inner edge of the D ring, so there are no internal criteria that can be used to evaluate the instrumental background levels in these images. To address this issue, we employ a high-phase D-ring profile derived from image W1500088644 (phase angle = 171°; see Hedman et al., 2007a). This profile extends beyond the inner edge of the D ring, enabling the instrumental background for this image to be removed and the relative brightness of different portions of the ring to be determined. If we plot the mean brightness measured for each of the above sequences versus the brightness of the ring in this reference profile, then we obtain a line whose y-intercept indicates the instrumental background level that should be subtracted from each data set. These levels are approximately one-half the brightness level in the D-ring's fainter regions.

Figs. 14 and 15 show the measured fractional amplitudes of the longitudinal brightness variations versus radius in the ring plane and the predicted perturbation periods assuming that the patterns are generated by 2:1 ILRs or 3:4 OLRs. The latter are computed based on Saturn's gravitational potential as given in Jacobson et al. (2006). In addition to individual curves for the different observations, these plots also show combined profiles that represent the weighted mean of the individual data sets (based on the errors in the variation amplitudes returned by the fitting program).

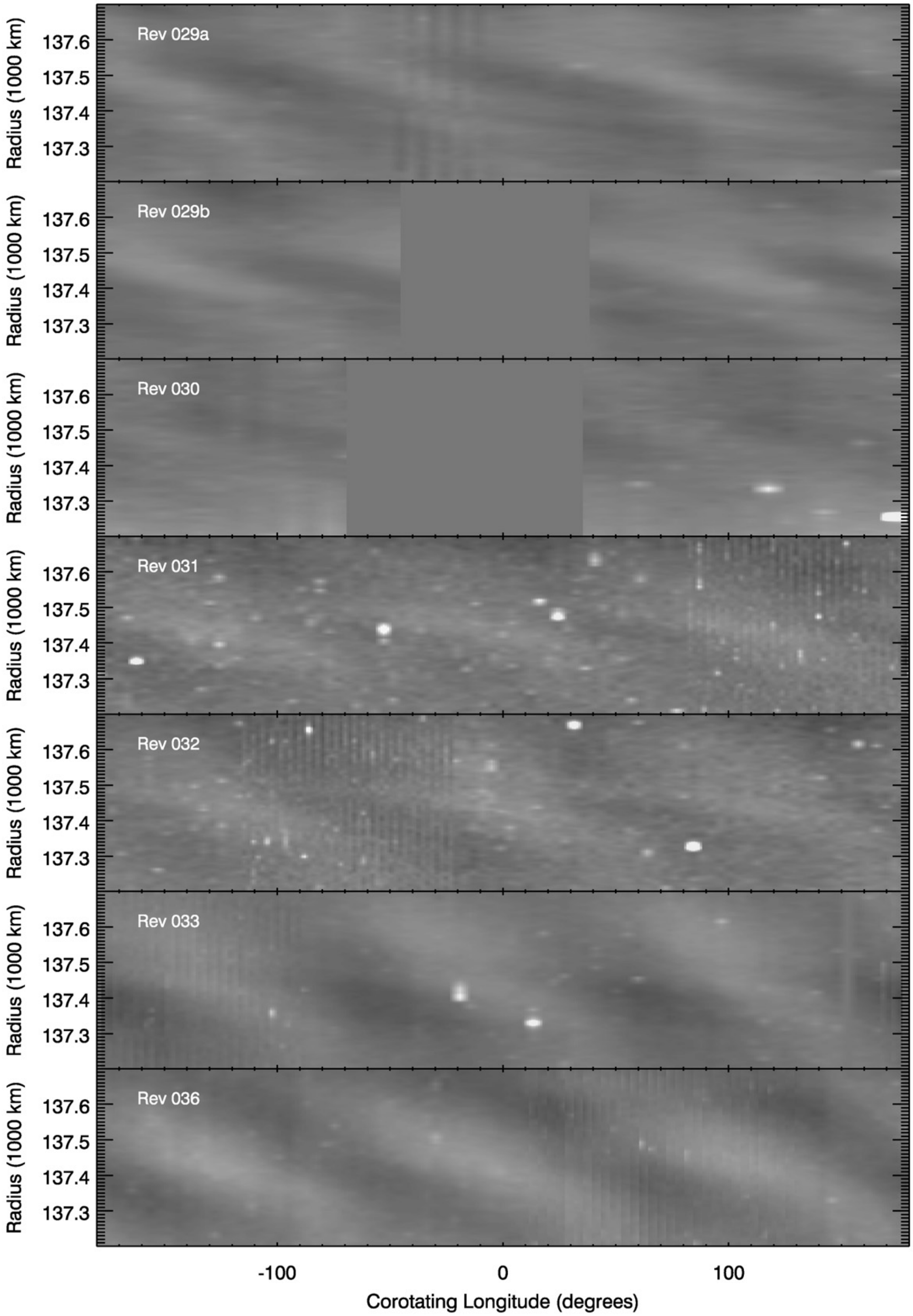

Fig. 12. A comparison of all the Roche Division data, precessed using a pattern period of 10.82 hours. Notice the pattern becomes more organized over time.

The D-ring data show multiple peaks in the amplitude at several distinct periods. Among the three different data sets, the Rev 43 curve is noticeably different from the Rev 37 and 39 profiles, which are very similar to each other. This probably occurs in part because the Rev 43 data were taken at a lower phase angle (see Table 1) which reduces the signal-to-noise. Furthermore, the spacecraft slewed over a range of longitudes during this observation, which introduces systematic drifts in the phase angle over the course of the observation that can lead to shifts in the ring brightness between the scans. Both of these phenomena may have intro-

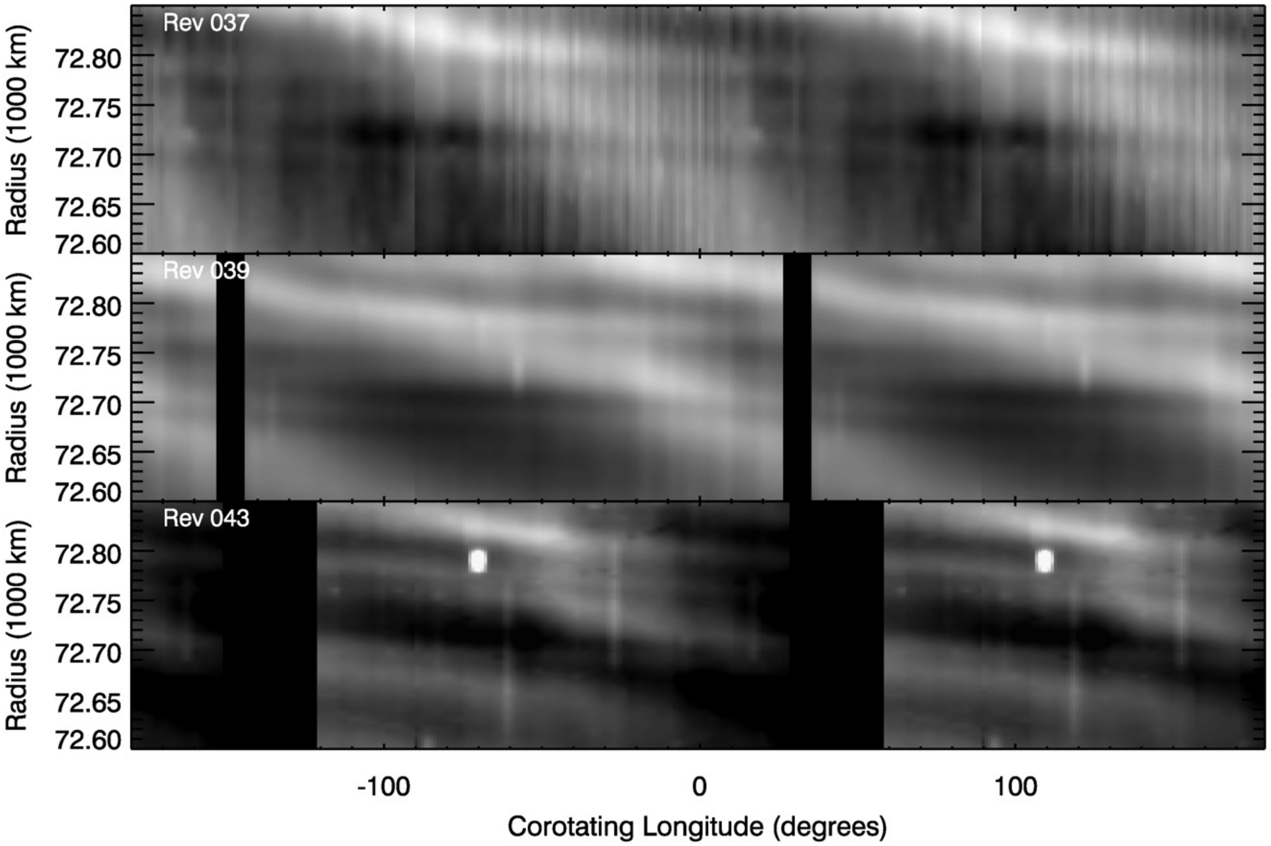

Fig. 13. D ring, precessed using the same longitude system as in the previous figure. The radial scale is chosen to match the range of pattern speeds covered in Figs. 10–12. Note the structure starts highly organized in Rev 37, but becomes less well organized by Rev 43.

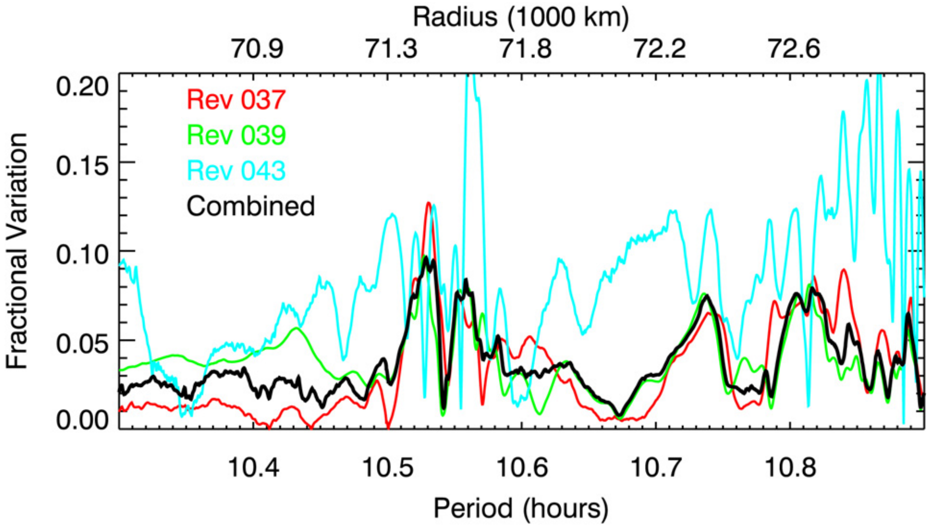

Fig. 14. Amplitude of the fractional brightness variations in the D ring versus radius in the ring (at top) and inferred perturbation period based on the expected pattern speed (at bottom). The combined (black) curve is the weighted mean of the three data sets. (For interpretation of the references to color in this figure legend, the reader is referred to the web version of this article.)

duced a higher background of spurious variations. However, some of the unique features in the Rev 43 data (such as the extremely strong peak at 71,700 km) may be due to temporal evolution of the patterns. As noted above, patterns at certain locations may become more or less prominent as various sub-patterns generated by multiple resonances drift past each other or as the strengths of the perturbation forces change. Such possibilities will clearly complicate any effort to isolate structures associated with closely spaced resonances. However, many of the broader, more prominent features in the earlier profiles (e.g., a peak around 71,500 km and a dip around 72,400 km) also appear in the Rev 43 data, so we should be able to reliably identify the gross properties of the dominant perturbation periods in this region.

The four most obvious peaks in the D ring data occur around 71,470; 71,600; 72,380, and 72,720 km. The two innermost features are very close together and so may represent a single complex of resonances centered around the D72 ringlet. The other two peaks lie within a sheet of material lying interior to D73. All four

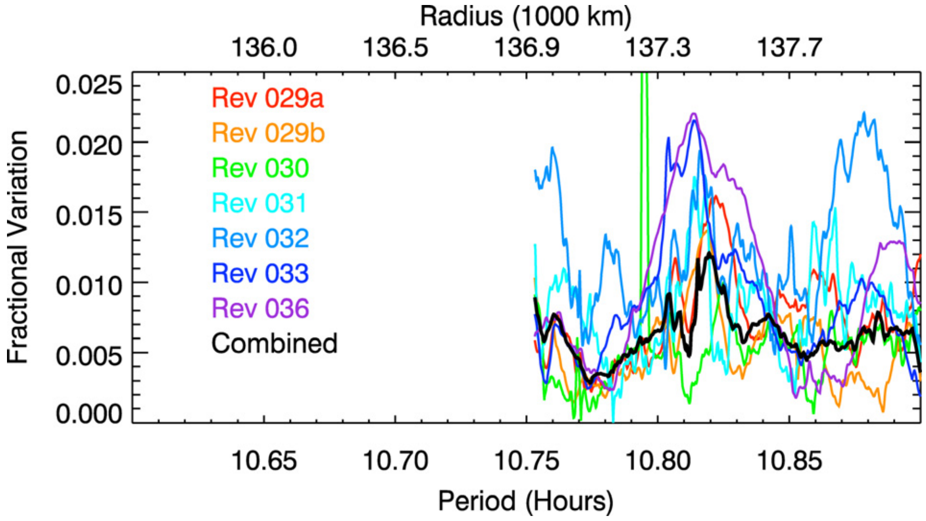

Fig. 15. Amplitude of the fractional brightness variations in the Roche Division versus radius in the ring (at top) and inferred perturbation period based on the expected pattern speed (at bottom). The (black) combined curve is the weighted mean of the individual data sets. These curves terminate at 136,900 km where the outer edge of the A ring begins.

Table 2
Strongest perturbations in the faint rings.

Location[a] a_r	Period[b]	Peak amplitude (A)	HWHM[c] L	τ	β[d] AL^2	Strength β/a_r^2
71470 km	10.52 hours 10.53 hours	0.095	60 km	14 days	340 km^2	6.6×10^{-8}
71600 km	10.56 hours	0.085	50 km	17 days	210 km^2	4.0×10^{-8}
72380 km	10.74 hours	0.075	90 km	10 days	600 km^2	11.4×10^{-8}
72720 km	10.81 hours 10.82 hours	0.080	90 km	10 days	650 km^2	12.3×10^{-8}
137460 km	10.82 hours	0.012	80 km	55 days	80 km^2	0.4×10^{-8}
169900 km	22.62 hours[e]	0.033	277 km	26 days	2600 km^2	9.0×10^{-8}

[a] Location of maxima in the amplitude of the fractional longitudinal brightness variations.

[b] Periods with the maxima of the consistency index; if two periods exist, both are given.

[c] HWHM defined as half the distance between the two points where the amplitude first falls below one-half its peak value.

[d] See Eq. (3).

[e] Orbital period of Mimas.

peaks have maximum fractional amplitudes of around 0.1 and half-widths between 50 and 100 km (see Table 2), although again we must caution that some of these features may be complexes produced by multiple resonances.

Turning to the Roche Division data, we find that practically all of the data sets yield one clear peak around 137,460 km (secondary peaks may also be present on either side of the main peak). While the position and amplitude of this peak vary somewhat from sequence to sequence, the average profile still shows a clear maximum with an amplitude of around 0.012. Note that the perturbation period required to generate this feature is around 10.82 hours, the same as the perturbation period required to explain the outermost feature in the D ring. This provides further evidence that both these patterns are produced by the same perturber.

4.2. *Period estimates from correlation coefficients*

The amplitudes of the brightness variations within individual observation sequences provide a relatively straightforward method for identifying the most perturbed regions in these rings. However, to obtain precise measurements of the dominant perturbation periods operating in these regions, one needs to compare observations from different times to determine how fast the relevant patterns are moving around Saturn.

Assuming a fixed pattern speed, we can map the data from multiple sequences onto a common co-rotating longitude system. After subtracting off a constant (Roche Division) or linear (D ring) background from each radial scan, the brightness versus co-rotating longitude at each radius typically has an approximately sinusoidal shape (see Fig. 18 below). If the assumed pattern speed is correct, the phase of the curves for different sequences would be the same. We evaluate how well the assumed pattern speed aligns the multiple data sets at each radius by computing the correlation coefficients between all possible pairs of longitudinal scans.

Fig. 16 illustrates the correlation coefficients computed for the D ring (the Roche Division data look similar). In this image, the correlation coefficients between different pairs of scans are shown as color intensity versus the assumed period and radius, which is measured relative to the expected location of the 2:1 ILR with the assumed period. White regions therefore indicate where all three correlation coefficients are high. At these locations the assumed pattern speed aligns the patterns in the different data sets well. Regions of strong correlation often form vertical bands in this image. These correspond to patterns extending over a finite radial range that move at single pattern speed. Note that all of these bright bands cross the line corresponding to $\delta r = 0$, which is the predicted location of the 2:1 Inner Lindblad Resonance for the given period. This not only supports our previous arguments that these patterns are due to 2:1 ILRs, but also verifies that our calculation of the pattern speeds for these structures is correct.

If the longitudinal profiles at each radius were purely sinusoidal, the correlation coefficient between any two data sets would be simply $\cos\delta\phi$, where $\delta\phi$ is the phase lag between the two sine curves in the two longitudinal profiles. We can therefore construct a statistic analogous to a χ^2 that measures the overall consistency of the profiles:

$$X^2 = \sum_{ij} \left[\cos^{-1}(C_{ij})\right]^2, \tag{30}$$

where C_{ij} is the correlation coefficient between observations i and j. For well-correlated data, $C_{ij} \simeq 1$ so this parameter is zero when the scans align perfectly and becomes more positive when the scans are less well aligned. Minima in this statistic therefore identify when the data at a radius are most consistent with a given pattern speed.

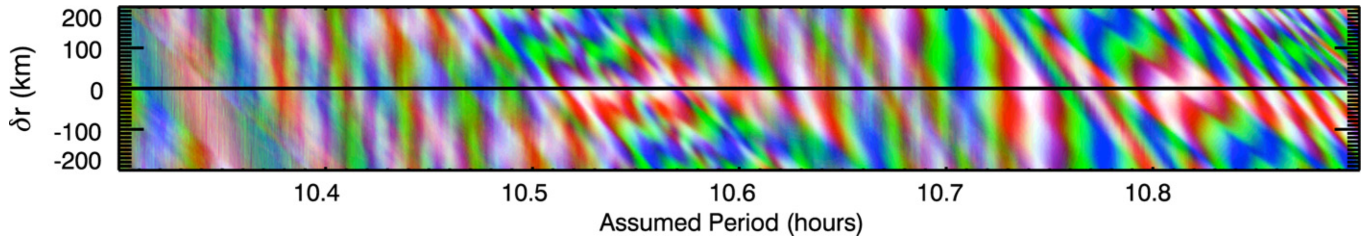

Fig. 16. Correlations between the three D-ring observations as a function of assumed period of the pattern and radius (measured relative to the expected location of the 2:1 ILR with the assumed period). Red, green and blue colors display the correlation coefficients between the Rev 37–Rev 39, Rev 37–Rev 43, and Rev 39–Rev 43 data. Brighter colors indicate stronger correlations, and white regions are zones where all three correlation coefficients are high so that the patterns are well aligned.

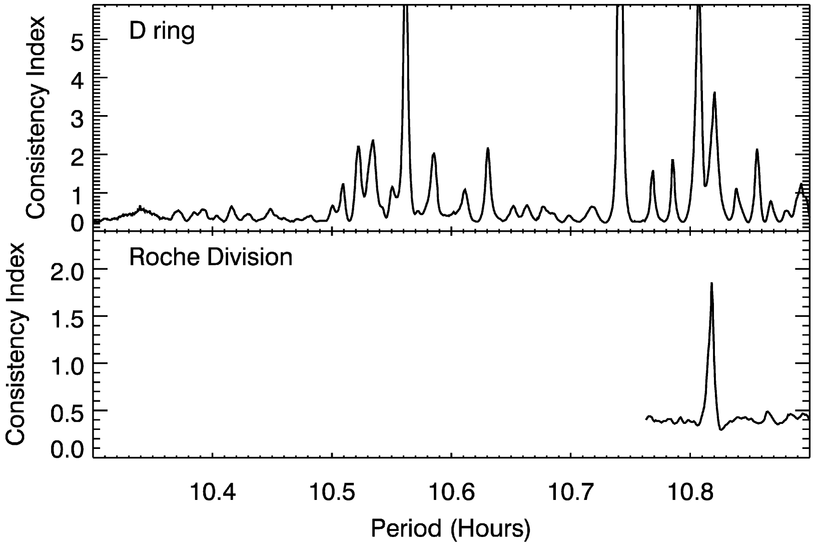

Fig. 17. Graphs of the consistency index for the D ring and the Roche Division as a function of period. The consistency index is a measure of how well the assumed period can fit the observed pattern at the expected location of the appropriate resonance with that period. The Roche Division and the D ring data show clear peaks at 10.82 hours, and the D ring data show additional peaks at various shorter periods. Compare with Figs. 14 and 15.

In order to display the goodness-of-fit of an assumed period to structures at different radii, we define the “consistency index” for a given period as the value of $1/X^2$ at the expected location of the appropriate resonance with that period. This parameter will have maxima near the location of any exact resonance in the ring. Note that the absolute magnitude of consistency index is not directly related to the strength of the resonance; instead it provides a measure of the pattern's persistence (the longer the pattern remains stable at a given speed, the higher the consistency index will be).

Fig. 17 shows the consistency index versus period for both the D ring and the Roche Division. Both regions show strong peaks in the consistency index near 10.82 hours, which matches the peak in the amplitude of the brightness variations seen in Figs. 14 and 15. Peaks in the D-ring's consistency index can also be observed at 10.53, 10.56 and 10.74 hours, corresponding to the other three maxima in the amplitude of the brightness variations (see Fig. 14). Note that while single peaks in the D-ring's consistency index appear at 10.56 and 10.74 hours, the maxima at 10.82 and 10.53 hours actually contain two closely spaced peaks. This could be due to slight shifts in the resonant periods over time, but also may simply be due to the relatively small number of data sets available for the D ring, which means that the time sampling for this region is very coarse. Indeed, the Roche Division observations, which include data from twice as many observing sequences, yield a better-defined peak at 10.82 hours.

Beyond the features associated with the amplitude maxima, several additional peaks in the D-ring's consistency index are present between 10.5 and 10.9 hours. These may represent weaker resonances in this ring. For example, the peak in the consistency index at 10.64 hours may be connected with a shoulder in the fractional amplitude visible at 71,900 km in Fig. 14. However, isolating these signals from nearby stronger resonant structures is challenging and therefore must be the subject of a future work.

5. Discussion

Table 2 summarizes the locations, perturbation periods, strengths and damping lengths of the strongest features discussed in this paper. The periods are derived from the locations of the peaks in the consistency index (Fig. 17), while the locations, amplitudes and half-width-at-half-maxima L are derived from the fractional longitudinal brightness variations (Figs. 14 and 15).

If we first consider the L-parameters, we find that all of the D-ring and Roche-division features have L values between 50 and 100 km, values of the same order of magnitude as the 280 km obtained above for the Mi 8:7 ILR in the G ring. If we convert these values of L into estimates of the eccentricity damping time $\tau = a_r/3n_rL$, we find that $\tau \sim 10$ days in the D ring, ~55 days in the Roche Division, and ~30 days in the G ring. Note that some of the features in the D ring and the Roche Division identified here as single resonances may in fact be complexes of multiple resonances, and thus would imply that the actual damping times are somewhat longer than the values reported here. Even so, it is remarkable that in all these regions the eccentricity-damping timescales are of order 10–100 days. This suggests that the damping mechanism is a widespread phenomena and may in fact be a generic feature of dusty rings.

Several different dissipative processes could affect the particle dynamics near these resonances (Meyer-Vernet and Sicardy, 1987), yielding patterns like those observed. However, the characteristics of the local ring material and the observed L values impose constraints on which physical mechanisms are most likely to be operating in these specific situations.

All of the resonant structures described here are in faint rings with very low optical depths, so it is relatively unlikely that collisions among particles within the ring are responsible for the dissipation. In particular, the part of the G ring containing the 8:7 Mimas resonance is almost an order of fainter than the brightest parts of this ring's arc, which have an estimated normal optical depth of 10^{-5} (Hedman et al., 2007b). Thus the region containing the resonance likely has an optical depth of order 10^{-6}. The critical disk optical depth for efficient collision dissipation at a $j : j-1$ satellite resonance derived by Goldreich and Tremaine (1980) is $\tau_{\text{crit}} = (M_{\text{satellite}}/M_{\text{Saturn}})^{2/3} j^{4/3}$. For this resonance, $\tau_{\text{crit}} \simeq 10^{-4}$, so interparticle collisions are probably not an important source of dissipation in this case. The situations in the D ring and the Roche Division are less clear-cut. These regions are 100–1000 times brighter than the G ring at comparable phase angles, which suggests that they have optical depths somewhere between 10^{-4} and 10^{-3}. These values are consistent with occultation measurements and limits of the D ring (Hedman et al., 2007a) and the Roche Division (Graps et al., 1984; Burns et al., 2001). Since we cannot easily define a critical optical depth in these regions because the resonances are not driven by known satellites, we cannot exclude the possibility that inter-particle collisions play some role in damping the orbital eccentricities near the resonance.

Although inter-particle interactions may occur near some of the resonances, we think it is more likely that the dominant dissipative process instead involves damping forces acting on individual particles. Recall that the particles in all these regions are strongly forward-scattering and therefore these rings are composed primarily of small (<100 μm) particles, which are sensitive to a wide range of non-gravitational forces, several of which can introduce dissipative terms in the equations of motion. The extremely short damping timescales implied by these observations can then help constrain which forces could be responsible for this damping. One candidate is resonant charge variations (Burns and Schaffer, 1989), where the charge on an eccentrically orbiting particle changes due to its varying velocity through the plasma; variations in the charge may also happen due to spatial variations in plasma properties with longitude or due to shadow passage. Such charge variations can lead to eccentricity damping if the charged particle is also embedded in a rotating magnetic field. Simulations show that in certain situations this mechanism can damp particle eccentricities on timescales comparable to those observed here (Burns and Schaffer, 1989).

Turning to the periods associated with the resonances in the D ring and Roche Division, we recognize that they are very close to the rotational periods of Saturn's winds and magnetic field. The observed cloud-tracked winds correspond to rotational periods between 10.2 and 10.7 hours, a range that includes the Voyager-era equatorial jet with a period of 10.2 hours (Sanchez-Lavega et al., 2000; Porco et al., 2005b). A bulk planetary rotation period of 10.54 hours minimizes the variations in the altitude of the 100-mbar isobaric surface derived from Voyager and Pioneer radio occultations (Anderson and Schubert, 2007). It is likely that the rotation of Saturn's deep interior lies close to this period or at least within the range of the cloud-tracked winds. The resonances in the D ring at 10.52–10.53 and 10.56 hours are close to this period, suggesting that some of the structure in the D ring may be sensitive to the rotation of Saturn's deep interior.

However, while there does seem to be a connection between the observed structures in the D ring and the planet, this connection does not appear to be direct but instead seems to be mediated by electromagnetic processes involving Saturn's magnetosphere. The D ring data clearly indicate that multiple perturbation periods affect the ring material, not a single frequency that could be ascribed unambiguously to the bulk rotation rate of the planet. Furthermore, f-mode acoustic oscillations like those suggested by Marley and Porco (1993) would each drive a single type of resonance in the vicinity of the D ring, and not a series of closely spaced 2:1 ILRs (also, Marley and Porco predicted the Lindblad-type resonances from these modes would be in the C ring, not the D ring nor the Roche Division).

The estimated strengths of the perturbations operating in the D ring and Roche division indicate that these forces are likely non-gravitational. Combining the peak amplitudes and HWHM in Table 2, we may compute the β-parameter and estimate the strength of the perturbations using Eq. (3). These estimates of the resonance strength suggest that the D-ring features may be driven by forces comparable to those generated by Mimas in the G ring (see Table 2). If these forces were gravitational, then comparably strong resonances should exist within the main rings, and such resonances would have dramatic effects on the rings (they would be comparable in strength to the 2:1 Inner Lindblad Resonance with Mimas that defines the inner edge of the B ring). These are not seen. If the forces involved are non-gravitational, then the lack of strong features in the main rings is not surprising because the main rings are composed primarily of centimeter-to-meter-sized particles that are much less sensitive to such forces than the <100 μm particles in the D ring and Roche Division. Furthermore, the 10.82-hour resonance in the D ring is about a factor of 30 times stronger than the comparable resonance in the Roche division, which is consistent with the large ratio in the predicted strengths of the 3:4 and 2:1 Lorentz resonances given in Burns et al. (1985). Thus, these rings are likely responding to periodic perturbations from Saturn's magnetosphere. These structures therefore may be driven by similar phenomena as those responsible for the periodic signatures in the spokes, which have comparable periods and are also composed primarily of small particles (Porco and Danielson, 1982; Porco, 1983).

Recent studies of periodic features in Saturn's radio emission strongly support a connection between periodic structures in the magnetosphere and these dusty rings. In a recent analysis of the Saturnian Kilometric Radiation (SKR), Kurth et al. (2008) report the detection of two distinct periods during late 2006 through early 2007 that are contemporaneous with the observations reported here. During this time interval, these two components of the SKR had periods of 10.80–10.83 hours ($n \sim 800°$/day) and 10.56–10.60 hours ($n \sim 815°$/day). These are extremely close to two of the strongest periods in the D ring, and the longer period matches the period seen in both the D ring and the Roche Division.

Kurth et al. (2008) also showed that the period of the 10.82-hour component has been changing over the course of the Cassini mission. These authors developed a longitude system that tracks this changing period throughout the duration of our observations, called SLS3. Fig. 18 shows brightness profiles near the peak of the 10.82-hour patterns from both the Roche Division and D ring in this coordinate system. All these scans are reasonably well aligned with each other in this coordinate system. This implies that these structures are moving around Saturn at roughly the same rate as this component of the SKR. This provides further confirmation that the patterns in the Roche Division are indeed driven by the same forces as those affecting the D ring. Furthermore, we note that both the Roche-Division and the D-ring profiles show brightness minima at $\sim -90°$. Recall that for moon-induced Lindblad resonances, one of the dark streaks should be aligned with the perturbing moon, where the radial pull of the moon is maximal. This implies that the particles in both these regions feel the maximum radial ac-

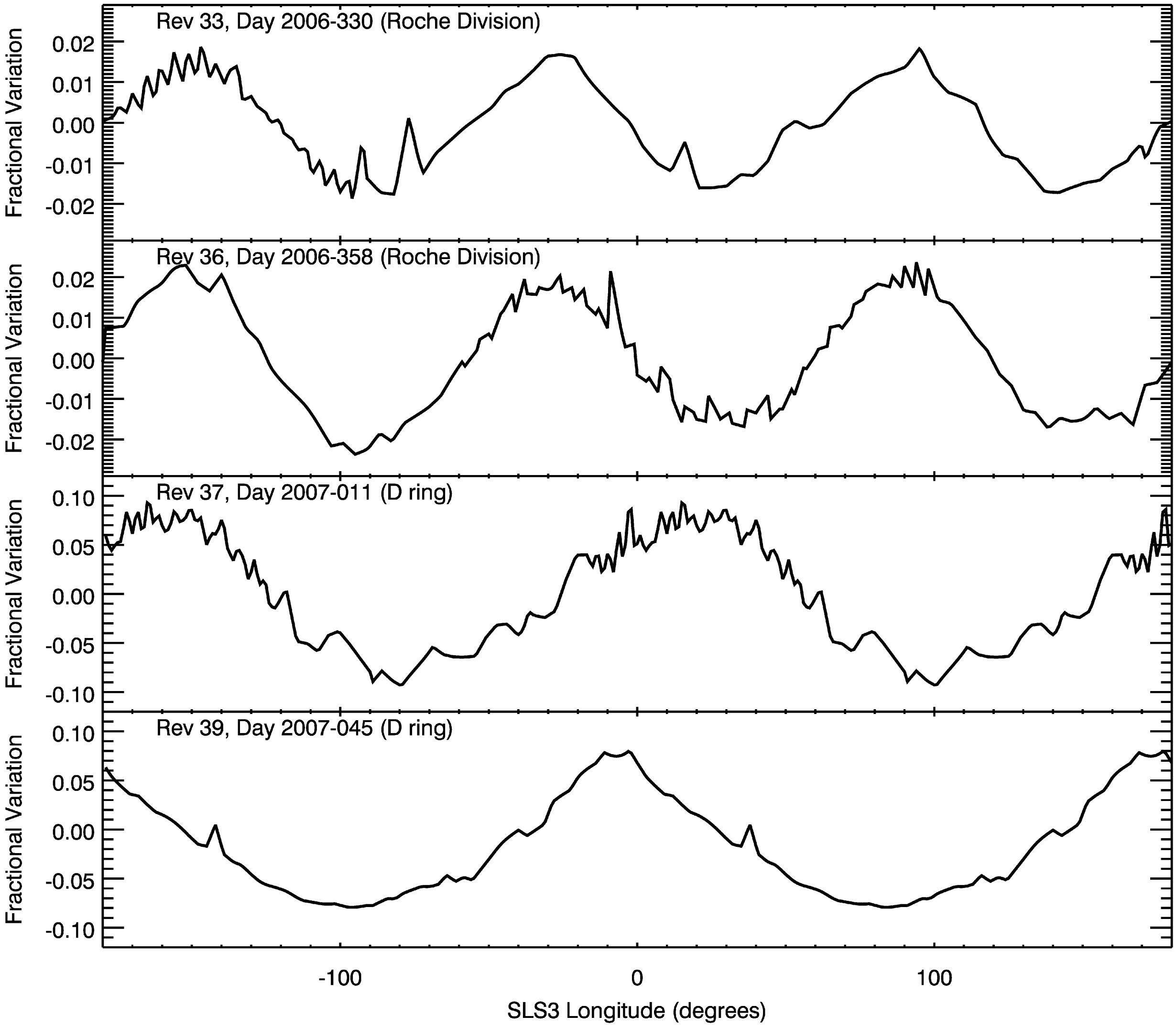

Fig. 18. Longitudinal brightness profiles of the Roche Division and D ring in the SLS3 coordinate system. Each curve is the average fractional brightness variation within ±20 km of the peak amplitude near 10.82 hours. Since the D ring data do not cover all longitudes in this system, for clarity these data are repeated twice assuming the brightness variations are $m = 2$ symmetric. Only data from Revs 33–39 are shown because at those times this pattern is strongest (see Figs. 12 and 13). Note that SLS3 is a left-handed coordinate system, which is opposite of the right-handed longitude systems displayed in previous figures.

celeration when they pass through this particular longitude in the SLS3 system.

While there is clearly a strong connection between these dusty rings and periodic variations in Saturn's radio emissions, the exact relationship between these phenomena remains unclear. The SLS3 longitude system organizes a number of other magnetospheric phenomena including variations in the magnetic field, plasma densities and energetic particle fluxes, and several models have been developed to explain these asymmetries in the magnetosphere by invoking various instabilities in the plasma flow near or outside the orbit of Enceladus (Gurnett et al., 2007; Goldreich and Farmer, 2007). However, it is not obvious how any of these asymmetries can perturb material as close to Saturn as the Roche Division and especially the D ring.

A thorough investigation of the possible physical mechanisms responsible for producing the observed structures in these faint rings is beyond the scope of this paper, but the location of the maximum radial acceleration in the SLS3 coordinate system should provide an important constraint on possible models. The SKR reaches its maximum intensity when the sun passes through +100° in this coordinate system, and during the Voyager era the maximum spoke activity occurred when this longitude passed through the morning terminator on the planet (Porco and Danielson, 1982). Furthermore, the azimuthal component of the magnetic field and the electron density measured by Cassini were maximal when the spacecraft passed through an SLS3 longitude of $\sim -30°$ (Gurnett et al., 2007), which is roughly on the opposite side of the planet and magnetosphere. The inferred longitude of maximum radial acceleration in the rings is closer to the latter than the former. While the implications of these relationships are still uncertain, it is likely that a full understanding of these features will provide insights into the dynamics of both these dusty rings and the magnetosphere as a whole.

Acknowledgments

The authors acknowledge support of NASA's Cassini Project, the Imaging Team and the Cassini Data Analysis Program. They also wish to thank P. Nicholson, A. Ingersoll, D. Gurnett, and W. Kurth for many useful conversations.

Appendix A. Maps of D ring and Roche Division

See Figs. 19–26.

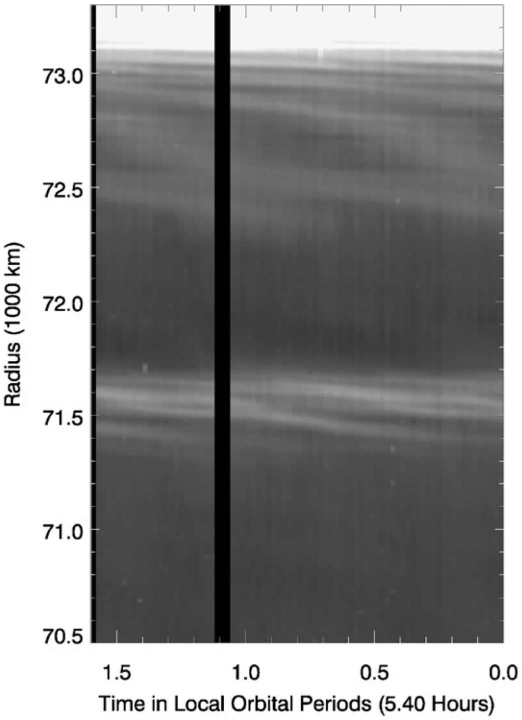

Fig. 19. Map of the middle D ring derived from the Rev 37 sequence, showing the brightness of the region at an inertial longitude of ~296° versus radius and time. Longitudinal brightness variations can be clearly seen around 71,500 km (i.e., the D72 ringlet) and between 72,500 and 73,000 km (just interior to D73). Note that a linear background has been subtracted from each radial scan used to form this image. The gap in the map corresponds to several images that have many missing lines.

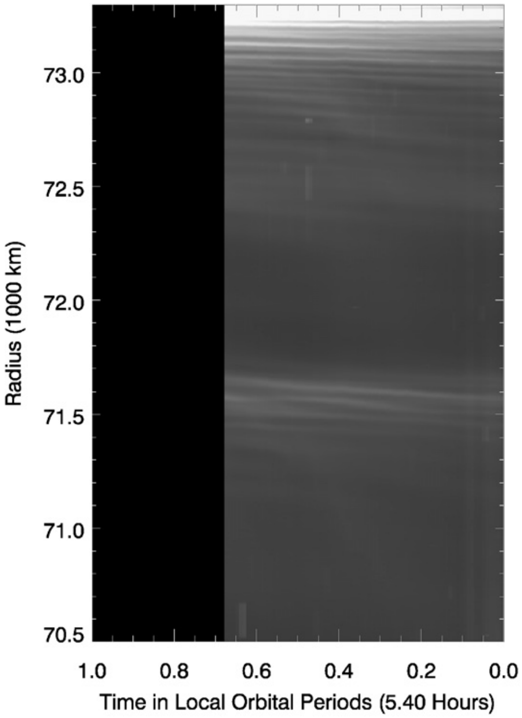

Fig. 20. Map of the middle D ring derived from the Rev 43 sequence, showing the brightness of the region at an inertial longitude observed by Cassini versus radius and time. Note that, unlike the other observations of the D ring, the images here observed a range of inertial longitudes (see Table 1), so features in this map cannot be directly compared with those in the other maps. Even so, longitudinal brightness variations can be clearly seen around 71,500 km (i.e., the D72 ringlet) and between 72,500 and 73,000 km (just interior to D73). Note that a linear background has been subtracted from each radial scan used to form this image.

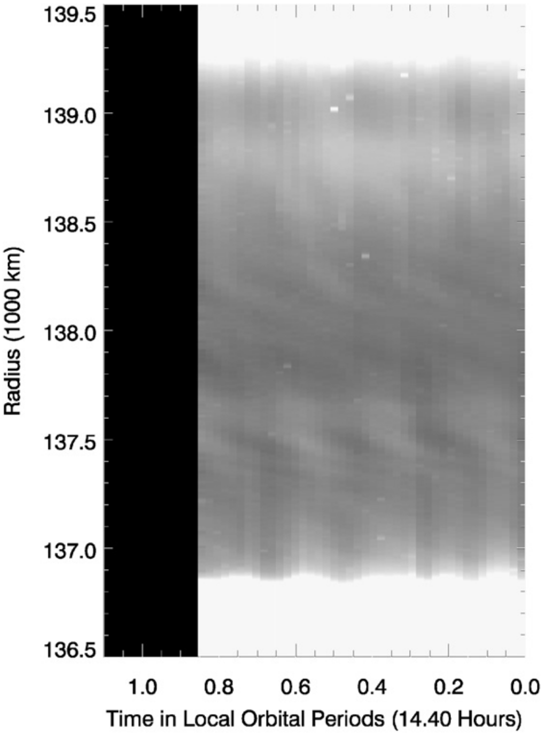

Fig. 21. Map of the Roche Division derived from the Rev 29a sequence, showing the brightness of this region at an inertial longitude of ~267° versus radius and time. Longitudinal brightness variations can be clearly seen between 137,000 and 138,200 km. Note that an average background level has been subtracted from each radial scan to make this image.

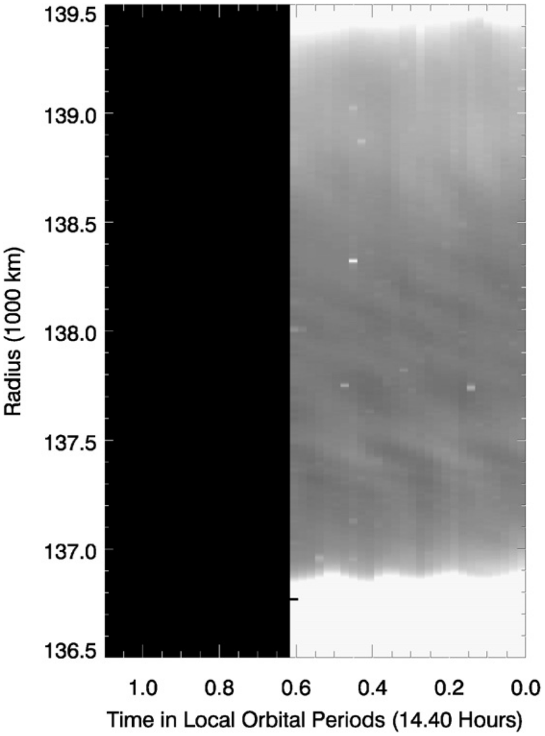

Fig. 22. Map of the Roche Division derived from the Rev 29b sequence, showing the brightness of this region at an inertial longitude of ~84° versus radius and time. Longitudinal brightness variations can be clearly seen between 137,000 and 138,200 km. Note that an average background level has been subtracted from each radial scan to make this image.

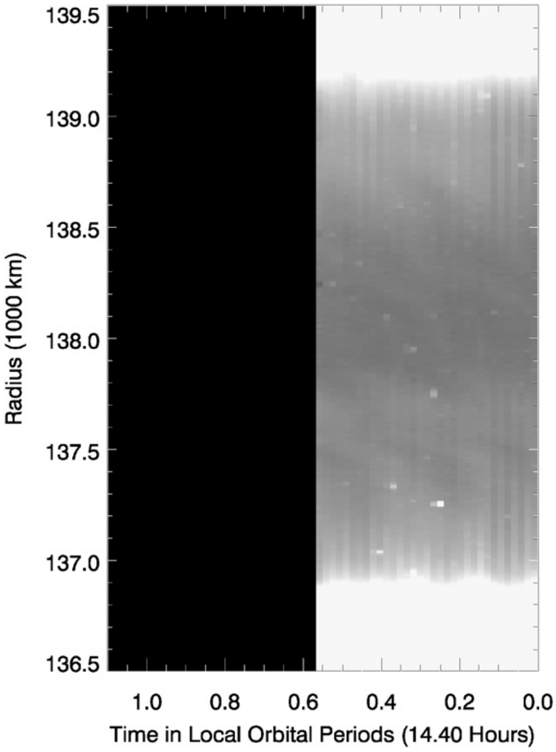

Fig. 23. Map of the Roche Division derived from the Rev 30 sequence, showing the brightness of this ring at an inertial longitude of ∼266° versus radius and time. Vertical banding is due to varying exposure levels used in these images. Longitudinal brightness variations can be seen between 137,000 and 138,200 km. Note that an average background level is subtracted from each radial scan to make this image.

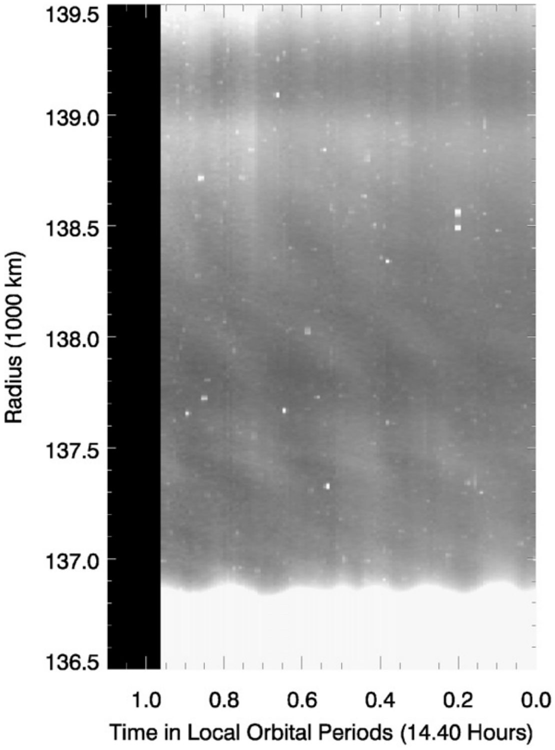

Fig. 25. Map of the Roche Division derived from the Rev 32 sequence, showing the brightness of this region at an inertial longitude of ∼96° versus radius and time. Vertical streaks that are most evident near the top of this image are due to features in the F ring (Murray et al., 2008). Longitudinal brightness variations can be clearly seen between 137,000 and 138,200 km. Note that an average background level has been subtracted from each radial scan to make this image.

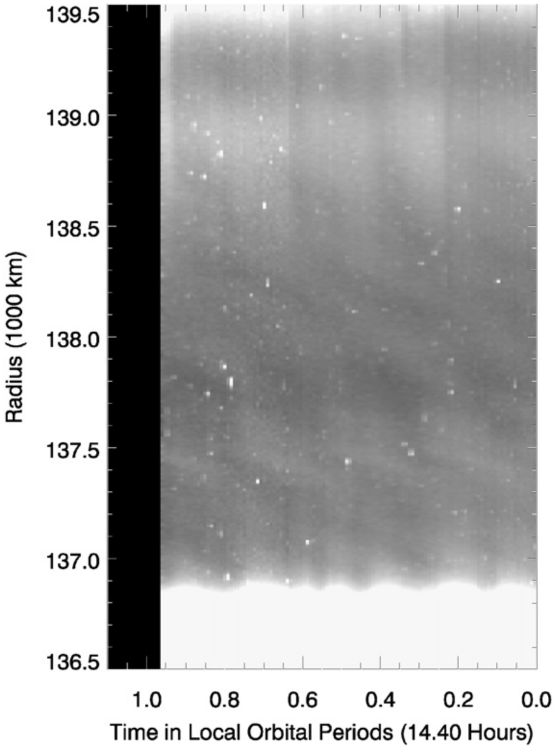

Fig. 24. Map of the Roche Division derived from the Rev 31 sequence, showing the brightness of this region at an inertial longitude of ∼96° versus radius and time. Vertical streaks near the top of this image are due to features in the F ring (Murray et al., 2008). Longitudinal brightness variations can be clearly seen between 137,000 and 138,200 km. Note that an average background level has been subtracted from each radial scan to make this image.

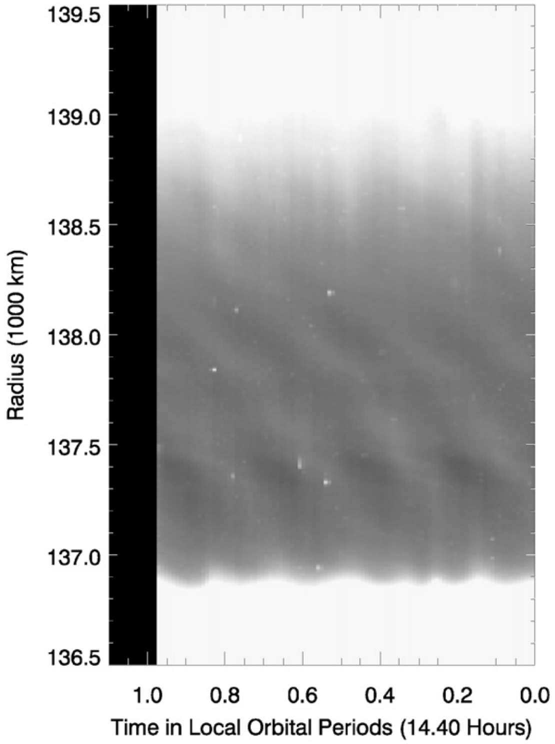

Fig. 26. Map of the Roche Division derived from the Rev 33 sequence, showing the brightness of this region at an inertial longitude of ∼296° versus radius and time. Vertical streaks near the top of this image are due to features in the F ring (Murray et al., 2008). Longitudinal brightness variations can be clearly seen between 137,000 and 138,200 km. Note that an average background level has been subtracted from each radial scan to make this image.

References

Anderson, J.D., Schubert, G., 2007. Saturn's gravitational field, internal rotation, and interior structure. Science 317, 1384–1387.

Baierlein, R., 1983. Newtonian Dynamics. McGraw–Hill, New York.

Burns, J.A., Schaffer, L., 1989. Orbital evolution of circumplanetary dust by resonant charge variations. Nature 337, 340–343.

Burns, J.A., Schaffer, L.E., Greenberg, R.J., Showalter, M.R., 1985. Lorentz resonances and the structure of the jovian ring. Nature 316, 115–119.

Burns, J.A., Hamilton, D.P., Showalter, M.R., 2001. Dusty rings and circumplanetary dust: Observations and simple physics. In: Grün, E., Gustafson, B.A.S., Dermott, S.F., Fechtig, H. (Eds.), Interplanetary Dust. Springer, Berlin, pp. 641–725.

Charnoz, S., Porco, C.C., Déau, E., Brahic, A., Spitale, J.N., Bacques, G., Baillie, K., 2005. Cassini discovers a kinematic spiral ring around Saturn. Science 310, 1300–1304.

Goldreich, P., Farmer, A.J., 2007. Spontaneous axisymmetry breaking of the external magnetic field at Saturn. J. Geophys. Res. (Space Phys.) 112 (A11), doi:10.1029/2006JA012163. 5225.

Goldreich, P., Tremaine, S., 1980. Disk–satellite interactions. Astrophys. J. 241, 425–441.

Goldreich, P., Tremaine, S., 1982. The dynamics of planetary rings. Annu. Rev. Astron. Astrophys. 20, 249–283.

Graps, A.L., Lane, A.L., Horn, L.J., Simmons, K.E., 1984. Evidence for material between Saturn's A and F rings from the Voyager 2 Photopolarimeter experiment. Icarus 60, 409–415.

Gurnett, D.A., Persoon, A.M., Kurth, W.S., Groene, J.B., Averkamp, T.F., Dougherty, M.K., Southwood, D.J., 2007. The variable rotation period of the inner region of Saturn's plasma disk. Science 316, 442–445.

Hamilton, D.P., 1994. A comparison of Lorentz, planetary gravitational, and satellite gravitational resonances. Icarus 109, 221–240.

Hañninen, J., Salo, H., 1992. Collisional simulations of satellite Lindblad resonances. Icarus 97, 228–247.

Hedman, M.M., Burns, J.A., Showalter, M.R., Porco, C.C., Nicholson, P.D., Bosh, A.S., Tiscareno, M.S., Brown, R.H., Buratti, B.J., Baines, K.H., Clark, R., 2007a. Saturn's dynamic D ring. Icarus 188, 89–107.

Hedman, M.M., Burns, J.A., Tiscareno, M.S., Porco, C.C., Jones, G.H., Roussos, E., Krupp, N., Paranicas, C., Kempf, S., 2007b. The source of Saturn's G ring. Science 317, 653–657.

Jacobson, R.A., Antreasian, P.G., Bordi, J.J., Criddle, K.E., Ionasescu, R., Jones, J.B., Mackenzie, R.A., Meek, M.C., Parcher, D., Pelletier, F.J., Owen Jr., W.M., Roth, D.C., Roundhill, I.M., Stauch, J.R., 2006. The gravity field of the saturnian system from satellite observations and spacecraft tracking data. Astron. J. 132, 2520–2526.

Kurth, W.S., Averkamp, T.F., Gurnett, D.A., Groene, J.B., Lecacheux, A., 2008. An update to a saturnian longitude system based on kilometric radio emissions. J. Geophys. Res. (Space Phys.) 113 (A12), doi:10.1029/2007JA012861. 5222.

Marley, M.S., Porco, C.C., 1993. Planetary acoustic mode seismology—Saturn's rings. Icarus 106, 508–524.

Meyer-Vernet, N., Sicardy, B., 1987. On the physics of resonant disk–satellite interaction. Icarus 69, 157–175.

Murray, C.D., Dermott, S.F., 1999. Solar System Dynamics. Cambridge University Press, Cambridge.

Murray, C.D., Beurle, K., Cooper, N.J., Evans, M.W., Williams, G.A., Charnoz, S., 2008. The determination of the structure of Saturn's F ring by nearby moonlets. Nature 453, 739–744.

Porco, C.C., 1983. Voyager observations of Saturn's rings. Ph.D. thesis, California Inst. of Technol., Pasadena.

Porco, C.C., Danielson, G.E., 1982. The periodic variation of spokes in Saturn's rings. Astron. J. 87, 826–833.

Porco, C.C., West, R.A., Squyres, S., McEwen, A., Thomas, P., Murray, C.D., Delgenio, A., Ingersoll, A.P., Johnson, T.V., Neukum, G., Veverka, J., Dones, L., Brahic, A., Burns, J.A., Haemmerle, V., Knowles, B., Dawson, D., Roatsch, T., Beurle, K., Owen, W., 2004. Cassini imaging science: Instrument characteristics and anticipated scientific investigations at Saturn. Space Sci. Rev. 115, 363–497.

Porco, C.C., Baker, E., Barbara, J., Beurle, K., Brahic, A., Burns, J.A., Charnoz, S., Cooper, N., Dawson, D.D., Del Genio, A.D., Denk, T., Dones, L., Dyudina, U., Evans, M.W., Giese, B., Grazier, K., Helfenstein, P., Ingersoll, A.P., Jacobson, R.A., Johnson, T.V., McEwen, A., Murray, C.D., Neukum, G., Owen, W.M., Perry, J., Roatsch, T., Spitale, J., Squyres, S., Thomas, P., Tiscareno, M., Turtle, E., Vasavada, A.R., Veverka, J., Wagner, R., West, R., 2005a. Cassini Imaging Science: Initial results on Saturn's rings and small satellites. Science 307, 1226–1236.

Porco, C.C., Baker, E., Barbara, J., Beurle, K., Brahic, A., Burns, J.A., Charnoz, S., Cooper, N., Dawson, D.D., Del Genio, A.D., Denk, T., Dones, L., Dyudina, U., Evans, M.W., Giese, B., Grazier, K., Helfenstein, P., Ingersoll, A.P., Jacobson, R.A., Johnson, T.V., McEwen, A., Murray, C.D., Neukum, G., Owen, W.M., Perry, J., Roatsch, T., Spitale, J., Squyres, S., Thomas, P., Tiscareno, M., Turtle, E., Vasavada, A.R., Veverka, J., Wagner, R., West, R., 2005b. Cassini Imaging Science: Initial results on Saturn's atmosphere. Science 307, 1243–1247.

Sanchez-Lavega, A., Rojas, J.F., Sada, P.V., 2000. Saturn's zonal winds at cloud level. Icarus 147, 405–420.

Shu, F.H., 1984. Waves in planetary rings. In: Greenberg, R., Brahic, A. (Eds.), Planetary Rings. University of Arizona Press, Tuscon, pp. 513–561.

Spitale, J.N., Porco, C.C., Colwell, J.E., Hahn, J.M., 2008. Kinematics of the outer edges of Saturn's A and B rings. Bull. Am. Astron. Soc. 39. Abstract 18.03.

Tiscareno, M.S., Burns, J.A., Nicholson, P.D., Hedman, M.M., Porco, C.C., 2007. Cassini imaging of Saturn's rings. II. A wavelet technique for analysis of density waves and other radial structure in the rings. Icarus 189, 14–34.

Wada, K., 1994. Gaseous orbits in a weak bar potential: Bar-driven spirals and effects of resonances. Publ. Astron. Soc. Jpn. 46, 165–172.